Magma evolution revealed by anorthite-rich plagioclase cumulate xenoliths from the Ontong Java Plateau: Insights into LIP magma dynamics and melt evolution

William S. Kinman *, Clive R. Neal

Department of Civil Engineering and Geological Sciences, University of Notre Dame, Notre Dame, IN 46556, USA

Abstract

Petrologic studies of igneous rocks often rely on whole-rock analyses alone to deduce source and melting histories. Whole-rock compositions represent a mixture of the processes responsible for the final texture and composition of the rock, but do not emphasize the evolutionary processes that the rock may have experienced. We examine the major, minor, and trace element compositions of plagioclase phenocrysts and plagioclase-rich cumulate xenoliths from a sequence of Kwaimbaita pillow basalt and massive flows recovered from Ocean Drilling Program (ODP) Site 1183 on the expansive ∼122 Ma Ontong Java Plateau (OJP) and from subaerial outcrops on the island of Malaita, Solomon Islands. These data are used to reconstruct equilibrium liquid compositions to understand magma dynamics, magma evolution, and the distribution basalt types across the OJP. Results reveal that crystals frequently are out of equilibrium with their host basalt. Two distinct compositional zones are present in plagioclase phenocrysts and xenolith crystals — An_{80-86} and An_{65-79}. Equilibrium magma compositions derived from each of these zones are distinct. In relative terms, the following distinctions are made:

An_{80-86}: Sr, Y, and Eu richer, Ba and LREE depleted, higher Sr/Ti, lower Ba/Sr and La/Y;
An_{65-79}: Sr, Y, and Eu poorer, Ba and LREE enriched, lower Sr/Ti, higher Ba/Sr and La/Y.

We observed several An_{65-79} parent magmas with higher La/Y, lower Sr, and higher LREE than the majority of An_{65-79} zones, which suggests that they grew from highly fractionated magmas. The An_{80-86} zones of both xenolith crystals and phenocrysts appear to have crystallized relatively early and are attributed to growth in magmas more primitive than parent magmas of An_{65-79} zones or the host magma. Using MELTS modeling we demonstrate a significant role for H_2O is not necessary to form An-rich crystals from known OJP magma types. These types of zones can instead form when relatively primitive OJP magmas ascend and partially crystallize at low pressures. Crystal mush layers are rheological elements of multiply saturated solidification fronts, and conditions for extreme fractionation are met deep with thermally and mechanically insulated mush-solidification fronts. Conditions in a homogenous magma body alone cannot generate the range of magma compositions and textures recorded in OJP plagioclase crystals. We suggest that the OJP magma chamber system consisted of crystal mush dominated regions and liquid dominated regions in a laterally and vertically extensive system of interconnected dikes and sills. Solidification front disruption was common during magma recharge and transport, which freed debris to mix with OJP magmas. The volume of crystalline debris from disrupted solidification fronts was small relative to the overall magma volume, which leads to little change of bulk magma chemistry. This can explain the dominance of the Kwaimbaita basalt type across the OJP. Evidence of solidification front disruption

---

* Corresponding author.
  E-mail address: kinman.1@nd.edu (W.S. Kinman).

is best preserved as allochthonous crystals both more and less primitive than bulk magma chemistry, both of which were observed in OJP basalts. Coincident with a zone of neutral buoyancy, the shallow OJP magma chamber system existed at a depth of 0–7 km. The OJP magma chamber system was thinner near the plateau margins, which provided less density filtration of magmas. This allowed more diverse magma types to reach the surface along the margins. It is envisaged that as the OJP formed, the zone of neutral buoyancy slowly migrated upward leading to slow yet pervasive assimilation of overlying seawater-altered basalt at the base of the lava pile.

1. Introduction

Petrologic studies have historically relied upon whole-rock chemistry alone to deduce evolutionary processes that modify magmas. Textural and microanalytical studies focused on plagioclase have been used to understand magma chamber processes and the chemical evolution of basaltic to silicic magmas (e.g., Davidson et al., 1998; Bindeman and Bailey, 1999; Bindeman and Davis, 2000; Tepley et al., 2000; Bryce and DePaolo, 2004). Plagioclase is well suited for microanalysis, as it contains measurable quantities of select incompatible trace elements, including the light rare earth elements (LREE). It is often preceded on the liquidus only by olivine, which does not appreciably fractionate the REE or other incompatible trace elements in the residual liquid (Bindeman and Bailey, 1999). We use major, minor, and trace element abundances measured in plagioclase by electron probe microanalysis (EPMA) and laser ablation ICP–MS (LA–ICP–MS) to invert chemical compositions of basaltic parental (equilibrium) magmas from a large igneous province (LIP) to investigate magma evolution. Accurate partition coefficient data are critical for this inversion. Plagioclase partition coefficients must be applied carefully because anorthite (An $= 100 * [Ca/(Ca + Na)]$) content is a controlling factor of cation substitution (Blundy and Wood, 1991; Bindeman et al., 1998). With accurate partition coefficients, inferred parent magma compositions provide insight into magma evolution beyond what is revealed by whole-rock data alone.

We examine basaltic magma evolution and magma chamber process of the Ontong Java Plateau (OJP), a mid-Cretaceous large igneous province (LIP) (Fig. 1). The uniformity of basalt composition over the Greenland-size OJP is remarkable (Neal et al., 1997; Tejada et al., 2002, 2004; Fitton and Goddard, 2004). Three different basalt types have been recovered from this vast LIP, and of these three types the Kwaimbaita basalt makes up >90% of the OJP (Neal et al., 1997; Tejada

et al., 2002, 2004). Our study is focused on plagioclase cumulate xenoliths from the Kwaimbaita basalt (Figs. 2 and 3). Kwaimbaita basalt is the only one of the three OJP basalt types that contains the xenoliths, and the magma chamber processes that produced this ubiquitous basalt type were the most common and important during formation of the OJP.

Previous studies have suggested that shallow (<6–8 km) fractional crystallization of olivine, plagioclase, and clinopyroxene was a major mechanism of OJP magma differentiation (e.g., Neal et al., 1997; Michael, 1999; Tejada et al., 2002; Fitton and Goddard, 2004; Roberge et al., 2004; Sano and Yamashita, 2004). Sano and Yamashita (2004) presented a magma chamber model to explain the narrow range of OJP basalt chemistry. An outstanding question in their study of OJP basalt petrography and phase equilibria was the origin of An-rich (>An$_{80}$) plagioclase, which they demonstrated through experiments to be out of equilibrium with Kwaimbaita basalt (Sano and Yamashita, 2004). We evaluate whether An-rich crystals grew in an evolved water-rich boundary layer, which is the model favored by Sano and Yamashita (2004), or whether they formed by an alternate process such as growth in a hotter more primitive magma. We also examine whether the uniform composition of large volumes of OJP basalt represents an averaging of more varied compositions, which may be reflective of important magma chamber processes. Finally, we examine how these processes relate to the spatial distribution of known basalt types across the OJP.

2. Geologic background of the Ontong Java Plateau

The Ontong Java Plateau is the world's largest oceanic LIP spanning an area of roughly 2.018×10^6 km^2 in the southwest Pacific Ocean (Mahoney et al., 1993a,b; Coffin and Eldholm, 1994; Tejada et al., 1996, 2002; M. Coffin, personal communication, 2003; Fig. 1). Tarduno et al. (1991) and Mahoney et al. (1993a,b)
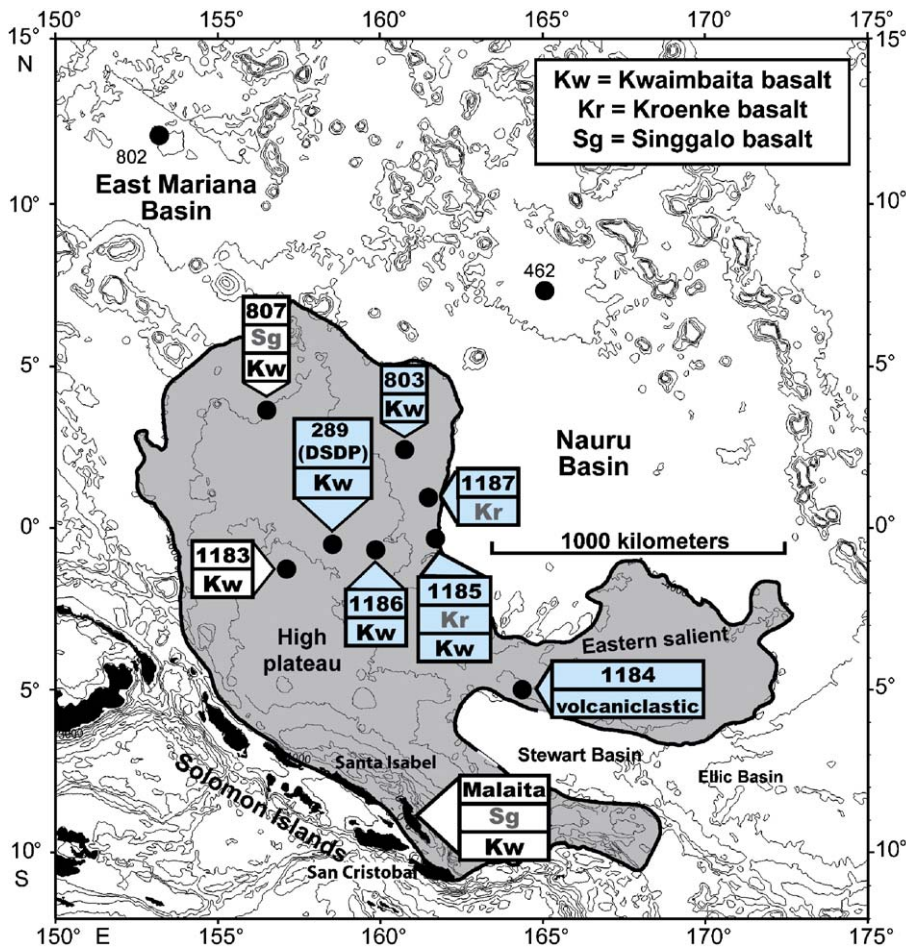
Fig. 1. Predicted bathymetry of the Ontong Java Plateau (OJP) (modified after Mahoney et al., 2001). The locations of Ocean Drilling Program (ODP) and Deep Sea Drilling Project (DSDP) drill sites on the OJP are shown with basalt types recovered at each location. Kw=Kwaimbaita basalt, Kr=Kroenke basalt, and Sg=Singgalo basalt.

suggested that the bulk of the OJP formed in a submarine eruptive environment relatively rapidly around ~122 Ma, with a minor event at ~90 Ma (Mahoney et al., 1993a, 2001; Tejada et al., 1996, 2002). Most of the OJP is presently submerged, exceptions being the southern plateau margin on the islands of Malaita, San Cristobal (Makira), and Santa Isabel in the Solomon Islands, where obducted segments now outcrop (Petterson et al., 1997; Fig. 1).

Despite its size, only three subtly different low-K tholeiitic basalt types have been recovered from the OJP, either by field work or ocean drilling, which have been referred to as Singgalo, Kwaimbaita, and Kroenke basalts (Tejada et al., 2002, 2004; Fitton and Goddard, 2004; Fig. 1). Singgalo basalts are isotopically distinct and overlie Kwaimbaita basalt on Malaita and ~1500 km to the north at Ocean Drilling Program (ODP) Site 807 (Mahoney et al., 1993a,b;

Neal et al., 1997; Tejada et al., 2002; Fig. 1). Incompatible trace element abundances are slightly enriched and MgO abundances lower (6–7.3%) in Singgalo basalts relative to Kwaimbaita basalts (7–8%) (Mahoney et al., 1993a,b; Tejada et al., 1996, 2002, 2004; Neal et al., 1997). Kroenke basalts have higher MgO (8–11 wt.%) and lower incompatible trace element abundances than Kwaimbaita basalts (Fitton and Goddard, 2004). However, these relatively primitive basalts are isotopically indistinguishable from the more fractionated Kwaimbaita basalts and share the same ~122 Ma age (Fitton and Goddard, 2004; Tejada et al., 2004). Fitton and Goddard (2004) and Tejada et al. (2004) suggested that Kroenke basalts are parental to Kwaimbaita basalts, being related by olivine fractionation. On the basis of current sampling Kroenke and Singgalo basalts represent minor components of the overall OJP volume and have been
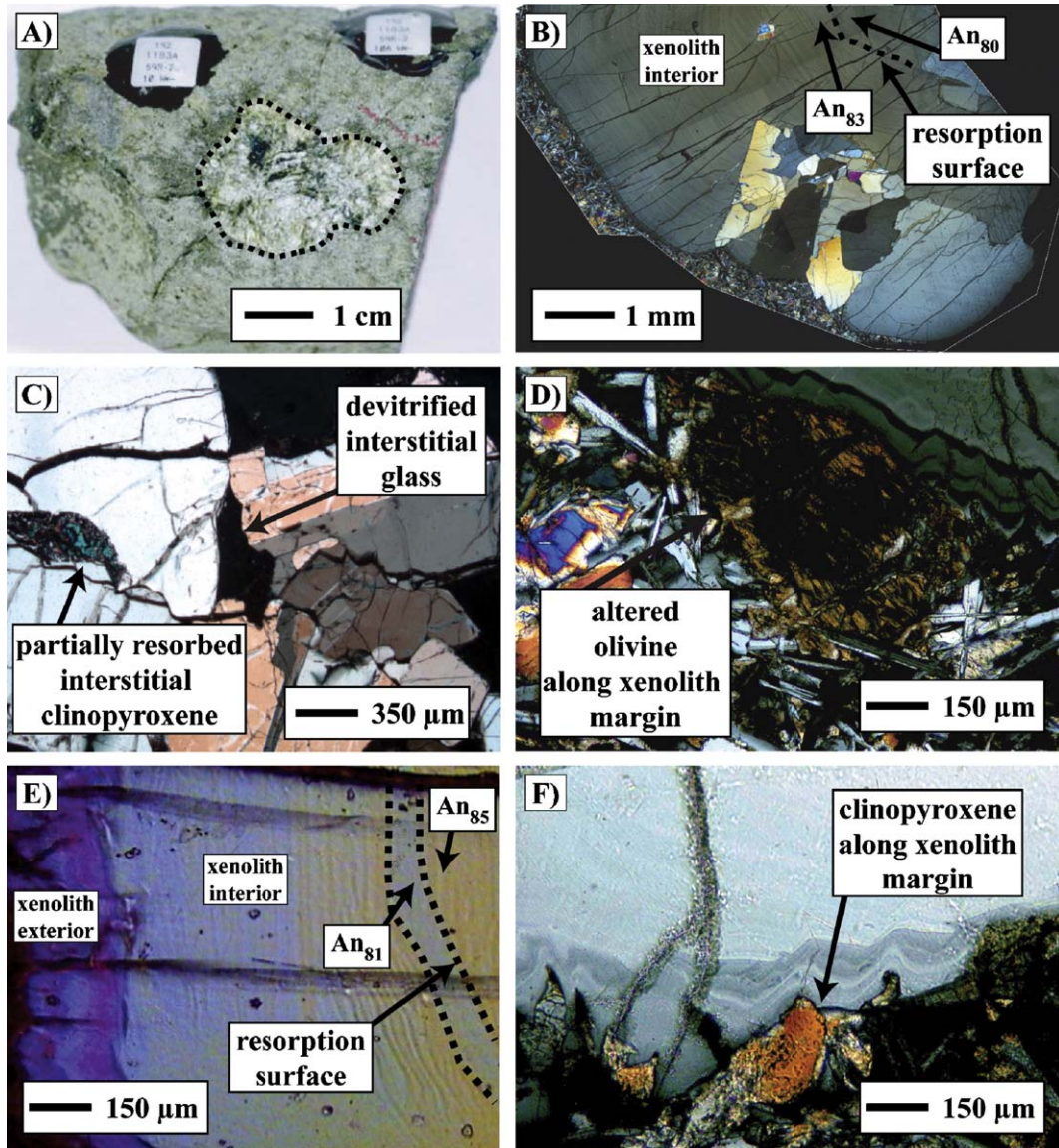
Fig. 2. Hand sample and thin section photographs of plagioclase-rich xenoliths hosted in Kwaimbaita basalt from ODP Site 1183. (A) Hand sample of Unit 5B xenolith (192-1183A-59R2 112–117cm piece #10A). (B) Mosaic photomicrograph of Unit 7 xenolith (192-1183A-64R2 116–120cm piece #9B). Note the network of plagioclase crystals and labeled resorption feature. All visible crystals are plagioclase. (C) Photomicrograph showing partially resorbed clinopyroxene and devitrified glass in a Unit 5B xenolith (adapted from Mahoney et al., 2001). (D) An altered olivine crystal along the margin of Unit 7 xenolith. (E) Photomicrograph of Unit 6 xenolith illustrating the xenolith interior and exterior and a resorption feature (192-1183A-63R2 25–27cm piece #4). (F) Photomicrograph of the margin of a Unit 6 xenolith. The xenolith exterior (i.e., rim) and a clinopyroxene crystal are visible.

recovered primarily from the margins of the plateau (Fitton and Goddard, 2004; Fig. 1).

3. Samples

The samples examined in this study were collected from outcrops along the Singgalo River on Malaita and by drill core at ODP Sites 807 (Leg 130) and 1183 (Leg 192), which are shown in Fig. 1 with the basalt types recovered at each location (see also Figs. 2 and 3). All xenolith crystals and phenocrysts examined in this study are from Kwaimbaita basalt and the ~122 Ma eruptive event (Mahoney et al., 1993a,b; Chambers et al., 2002; Tejada et al., 2002, 2004; Fitton and Goddard, 2004). Malaita is located along the southern margin of the plateau (see Figs. 1 and 3). Site 807 is along the northern
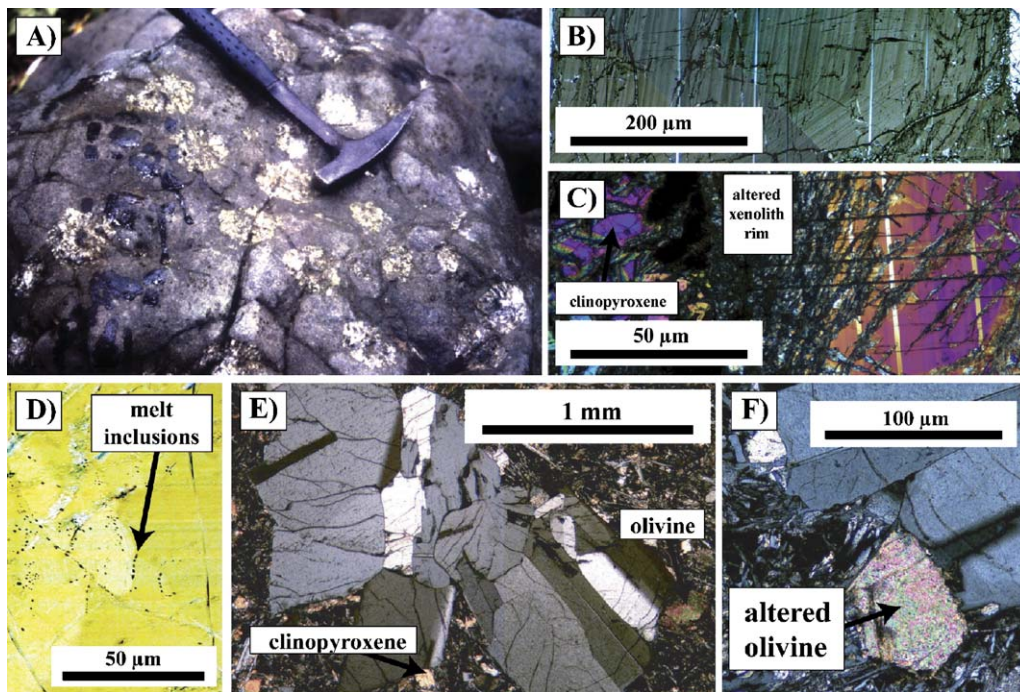
Fig. 3. Hand sample and thin section photographs of plagioclase-rich xenoliths hosted in Kwaimbaita basalt from ODP Site 807 and Malaita. (A) A boulder of Kwaimbaita basalt (SGB-21) from along the Singgalo River, Malaita exhibiting large plagioclase-rich xenoliths. Note the rock hammer for scale. (B) Mosaic photomicrograph of the interior of Malaita xenolith ML-X1, exhibiting oscillatory zoning. (C) Rim of xenolith ML-X1 illustrating destruction of the rim zones by alteration and a clinopyroxene crystal present along the rim. (D) Small melt inclusions within ML-X1 that run parallel to zoning features. (E) Mosaic photomicrograph of xenolith 807-X1 from ODP Site 807 (130-807C-93R-1-137-139). Note: olivine and clinopyroxene along the xenolith margins. (F) Altered olivine along the margin of 807-X1.

margin of the OJP, and the xenoliths are from Units C–G, which are equivalent to the Kwaimbaita basalts (Figs. 1 and 3). Site 1183 is near the bathymetric high of the plateau, where 80.7 m of Kwaimbaita pillow basalt was cored, representing 8 flow units (Mahoney et al., 2001; Fig. 4). Plagioclase cumulate xenoliths (Fig. 2) are found in all but Unit 1 of the cored section at Site 1183 (Mahoney et al., 2001; Fig. 4). Kwaimbaita basalt is found as massive and pillow basalt flows, generally has a subophitic to intergranular texture, and <2% (volume) phenocrysts (Mahoney et al., 2001; Tejada et al., 2002; Sano and Yamashita, 2004). The dominant phenocrysts in Kwaimbaita basalts are olivine and plagioclase with lesser amounts of clinopyroxene.

We measured major and trace elements in single large crystals from one Malaitan xenolith (host basalt SGB-21, cf., Tejada et al., 2002; Fig. 3A–D), from three Site 1183 xenoliths (Units 5B, 6, and 7; see Fig. 2), and from a single glomerocryst/xenolith from Site 807 (Fig. 3E). We also measured major and trace element data at select points in a variety of phenocrysts from Site 1183 Units 5B, 6, and 7 basalts (Fig. 5). We did not examine any plagioclase phenocrysts from Kwaimbaita basalt SGB-21 from Malaita or the Site 807 Kwaimbaita basalt. Detailed descriptions of zoning patterns of the xenolith plagioclase crystals and phenocrysts are provided in the Results section.

3.1. A cogenetic relationship between xenoliths?

Isotopic studies were not conducted on any of the plagioclase crystals in this study. Tejada et al. (2002) reported isotopic data for a single OJP plagioclase xenolith, which was isotopically indistinguishable from its Kwaimbaita host basalt (SGB-21, see sample description below). We therefore assume for this study that the plagioclase-rich xenoliths, all in Kwaimbaita host basalt, are indistinguishable from Kwaimbaita-type basalt.

4. Methods

4.1. Analytical methods

Samples were prepared as polished thick sections (80–100 μm) with Bi-doped epoxy to signal when the sample had been penetrated during LA–ICP–MS
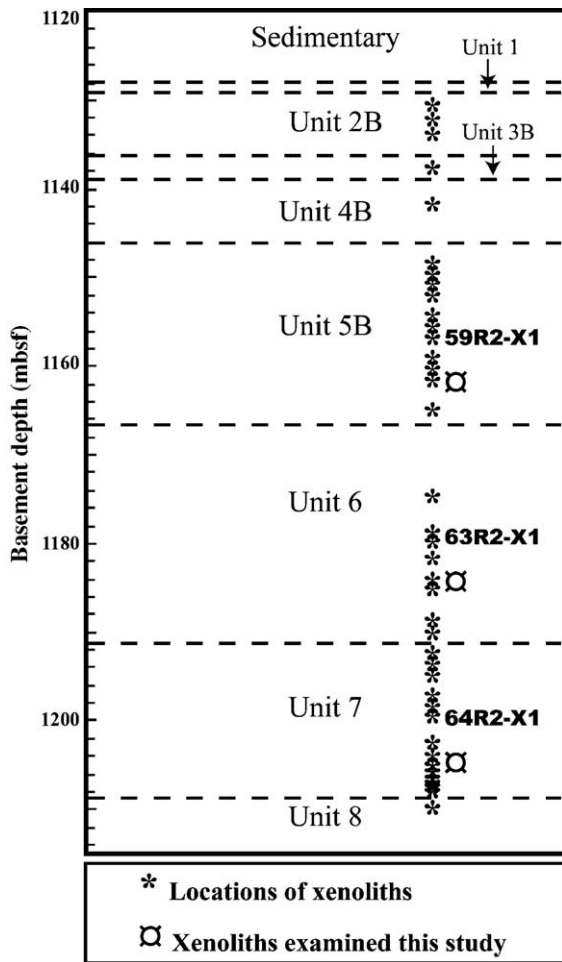
Fig. 4. Stratigraphic section of basaltic basement cored at ODP Site 1183 consisting entirely of Kwaimbaita pillow basalt flow units. The locations of xenoliths are labeled with asterisks. The locations of xenoliths examined in this study (59R2-X1, 63R2-X1, and 64R2-X1) are labeled.

inclusions and alteration-filled fractures were discarded due to Fe fluorescence effects. Titanium was quantified by EPMA.

Sr, Y, Ba, La, Ce, Nd, and Eu were measured in plagioclase crystals using a New Wave UP-213 UV laser ablation system interfaced with a ThermoFinnigan Element 2 ICP-MS operated in fast magnet scanning mode at the University of Notre Dame. We used a laser frequency of 4 Hz, pulse energy of 0.02–0.03 mJ pulse^{-1}, 12 or 20 μm diameter pits depending on crystal size, and helium as the carrier gas (~ 0.71 min^{-1}) mixed with argon (~ 1.01 min^{-1}) before its introduction to the plasma. Analyses were conducted in peak jumping mode with one point quantified per mass. The LA–ICP–MS spots were coincident with previous EPMA analyses, and Ca measured by EPMA was used as an internal standard for each spot analysis. The trace element glass NIST 612 was used as a calibration standard in all laser ablation analyses. Although heterogeneity for certain elements has been documented in the widely used NIST 612 glass (i.e., Eggins and Shelly, 2002), Eggins and Shelly (2002) considered it a reliable calibration standard for Sr, Ba, Y, and the REE. The methods of Longerich et al. (1996) and Norman et al. (1996) were used to reduce LA–ICP–MS data and calculate analytical uncertainty for each spot analysis (see Table 1).

4.2. Data quality

The quality of EPMA data were monitored by major element and cation totals. Data points where major element totals were greater than 101.5% or less than 98.5% are not used in further discussion nor are points with cation totals greater or less than 20 ± 0.1 cations (based on 32 O). All laser ablation analyses were collected in time-resolved mode so that signal from inclusions and alteration-filled fractures could be easily excluded. Results from laser ablation spots close to fractures or that penetrated into underlying fractures were discarded. The rate of laser ablation was tested using a 100-μm-thick plagioclase wafer prior to sampling, which allowed optimization of operating conditions to yield desired sensitivity and sampling depth (<30 μm).

4.3. Choosing partition coefficients (D)

Blundy (1997) concluded that inversion of magma compositions from mineral data using appropriate D values to be a robust means of estimating parent magma compositions and suggested that D values derived from microbeam techniques were more accurate than those derived from bulk crystal-matrix analyses. Bindeman

analyses (e.g., Jefferies et al., 1998). Bismuth was chosen as a dopant because naturally occurring Bi is well below analytical detection limits in plagioclase. Backscatter electron images and major element analyses were performed using a JEOL JXA-8600 Superprobe electron microprobe at the University of Notre Dame. Backscatter electron images were taken using a 1 μm beam, an accelerating voltage of 20 kV, and a probe current of 25–50 nA. Microprobe analyses were performed using a 5 μm defocused beam, accelerating voltage of 15 or 20 kV depending upon samples, a probe current of 20 nA, 15 s on-peak counting time, and two background measurements per peak. We measured Na first to minimize loss via volatilization. Microprobe data were corrected for matrix effects using a ZAF correction method. Data points near Fe-rich phases such as melt
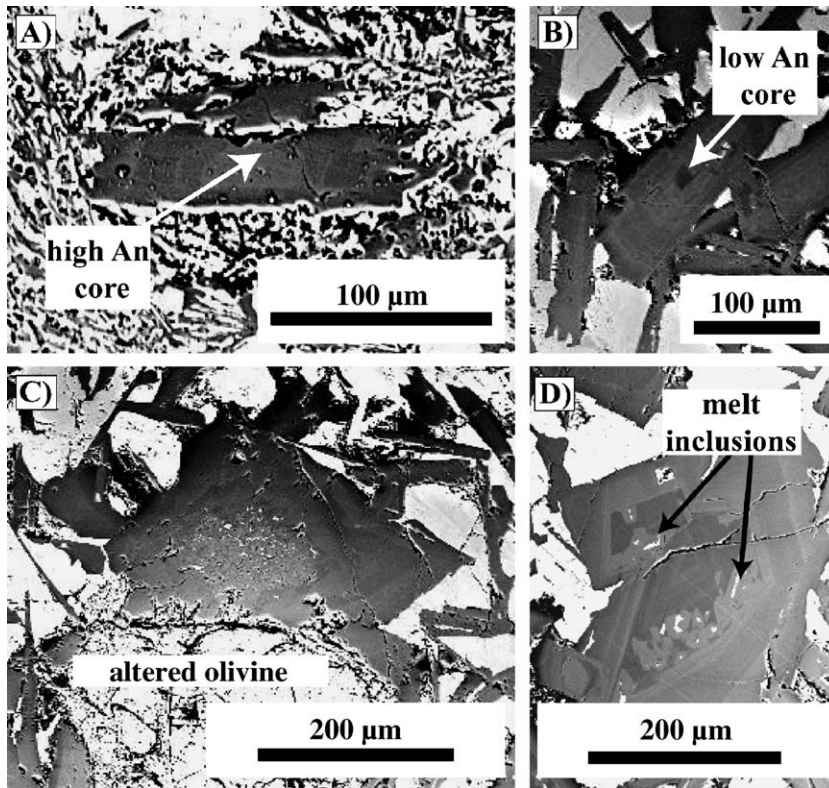
Fig. 5. Backscatter electron images of plagioclase phenocrysts from Site 1183 basalts. (A) A Type I normal zoned crystal (63R2-P4, Unit 6). Note the brighter, higher An core. (B) A Type II reverse zoned crystal with a darker, lower An core (64R2-P4, Unit 7). (C) An olivine–plagioclase glomerocryst (64R2-P3, Unit 7). The plagioclase crystal has a sieve textured core. (D) A reverse zoned Type II crystal that contains numerous melt inclusions (64R2-P1).

and Davis (2000) noted that D values derived from doping experiments should be used with caution as, for example, the D_{REE} and D_Y in REE-doped runs are 30–100% higher than in undoped runs. Blundy and Wood (1991) and Bindeman et al. (1998) showed that the dominant factors controlling the trace element D values for plagioclase are An content and crystallization temperature (pressure effects appeared to be negligible). Bindeman et al. (1998) applied this relationship to a wide variety of trace elements and produced values for the constants "a" and "b" in their Eq. (2) for calculating plagioclase partition coefficients via the expression:

$$RT\ln(D_i) = aX_{An} + b \qquad (1)$$

where R is the gas constant, T is temperature (K), and X_{An} is the mole fraction of anorthite in the plagioclase. Using Eq. (1), Ginibre et al. (2002) noted that temperatures in the range of 850–1000 °C had only a small effect on calculated melt concentrations for Sr and Ba (within their analytical uncertainty). Likewise, Bindeman et al. (1998) showed that variations

~ 150 °C produce <10% differences for particular partition coefficients, which were often within error of the respective D values.

4.4. Partition coefficients for OJP plagioclase crystals

We used the equations and constants of Bindeman et al. (1998), derived from partitioning experiments run at natural (i.e., undoped) trace element concentration levels at atmospheric pressure, to calculate D values for Sr, Y, Ba, La, Ce, Nd, and Ti (see Table 3). We assumed a crystallization temperature of 1185 °C to calculate D values. Sano and Yamashita (2004) reported initial crystallization of plagioclase at 1170 °C from Kwaimbaita-type magmas and 1200 °C from more primitive Kroenke-type magmas. The use of 1170 vs. 1200 °C in D calculations yields <4% differences in trace element concentrations of parent liquids, within the analytical error for most of our analyses. We neglect pressure effects since they are not well documented for most elements, and where they were documented for D_{Sr} by Vander Auwera et al. (2000) they were negligible.

Table 1

Major and trace element data of plagioclase as phenocrysts in the host basalt and in the xenoliths

Crystal zone	An (mol%)	SiO_2	TiO_2	Al_2O_3	FeO_T	MgO	CaO	Na_2O	K_2O	P_2O_5	Total	Sr	Y	Ba	La	Ce	Nd	Eu
ML-X1 xenolith																		
Interior	85	47.5	0.02	31.9	0.54	0.22	17.4	1.71	0.07	0.17	100.8	172.4±5.0	0.21±0.10	2.31±0.38	0.24±0.08	0.59±0.11	–	0.25±0.11
Interior	85	48.0	0.01	32.4	0.55	0.23	17.5	1.67	–	0.13	100.5	161.3±7.3	0.18±0.09	2.99±0.33	0.17±0.08	0.25±0.06	0.37±0.17	0.34±0.14
Interior	85	47.7	0.02	31.4	0.52	0.23	17.3	1.65	0.05	0.17	100.5	176.9±7.7	0.19±0.09	1.93±0.37	0.20±0.10	0.37±0.09	0.39±0.21	0.35±0.16
Interior	86	47.6	0.01	32.2	0.56	0.23	17.7	1.63	0.04	0.13	100.4	187.0±10.2	0.13±0.11	2.18±0.50	0.25±0.10	0.36±0.09	0.76±0.27	0.42±0.24
Interior	84	48.0	0.01	31.7	0.56	0.25	17.4	1.79	0.09	0.13	100.4	172.7±7.2	–	2.90±0.38	0.39±0.12	0.36±0.11	0.38±0.16	0.47±0.15
Interior	86	47.7	0.03	32.6	0.56	0.23	18.1	1.57	0.03	0.17	99.8	185.3±4.3	0.43±0.15	3.12±0.37	0.30±0.14	0.54±0.09	0.23±0.21	–
59R2-X1 xenolith																		
Exterior	66	55.4	0.03	26.2	1.01	0.21	13.4	3.67	0.15	0.16	100.2	–	–	–	–	–	–	–
Exterior	75	50.6	0.04	29.6	0.72	0.32	16.1	3.98	0.03	0.13	100.5	225.7±5.0	0.19±0.05	4.97±0.38	0.43±0.07	0.65±0.06	0.49±0.14	0.49±0.06
Interior	81	49.3	0.02	30.1	0.65	0.26	17.5	2.32	0.03	0.18	100.4	–	–	–	–	–	–	–
Interior	82	50.2	0.03	29.4	0.70	0.27	17.8	2.18	0.01	0.17	100.8	199.7±3.8	0.14±0.04	3.84±0.20	0.27±0.04	0.57±0.06	0.30±0.12	0.45±0.06
Interior	83	48.8	0.02	31.0	0.65	0.24	17.6	1.94	0.01	0.15	100.4	218.7±6.5	0.18±0.05	4.65±0.42	0.22±0.04	0.57±0.06	0.52±0.14	0.45±0.07
Interior	82	49.5	0.01	29.8	0.67	0.28	17.8	2.11	0.02	0.21	100.4	203.5±4.5	0.12±0.04	3.64±0.26	0.20±0.05	0.61±0.08	0.42±0.13	0.47±0.07
Center/core	83	48.8	0.01	30.7	0.66	0.25	18.0	1.98	0.02	0.14	100.5	206.0±4.8	0.19±0.04	5.05±1.29	0.31±0.05	0.58±0.07	0.64±0.13	0.34±0.05
59R2 phenocrysts P1–P4																		
P1 rim	71	51.7	0.03	27.8	0.84	0.33	15.0	3.35	0.02	0.16	99.3	202.2±6.9	0.29±0.05	6.06±0.55	0.35±0.10	0.70±0.09	0.78±0.23	0.38±0.08
P1 core	74	51.0	0.03	29.4	0.74	0.28	15.4	2.97	0.01	0.12	100.0	187.4±5.0	0.13±0.05	4.30±0.36	0.36±0.05	0.54±0.07	0.42±0.16	0.42±0.04
P2 rim	70	51.4	0.04	29.2	0.84	0.33	14.8	3.44	0.02	0.12	100.3	207.1±7.1	0.22±0.06	5.26±0.47	0.39±0.06	0.71±0.10	0.46±0.15	0.47±0.07
P2 core	73	51.2	0.03	29.2	0.75	0.34	15.5	3.13	0.02	0.15	100.3	195.4±6.9	0.34±0.07	4.56±0.37	0.46±0.07	0.52±0.07	0.47±0.15	0.39±0.06
P3 center	69	51.0	0.03	29.4	0.85	0.34	14.3	3.50	0.03	0.14	99.6	–	–	–	–	–	–	–
P4 center	67	52.1	0.03	28.6	0.89	0.37	13.7	3.77	0.03	0.15	99.7	–	–	–	–	–	–	–
63R2-X1 xenolith																		
Exterior	79	47.6	0.03	31.2	0.74	0.28	17.4	2.32	0.02	0.22	99.9	178.1±3.6	0.27±0.08	3.04±0.22	0.20±0.08	0.43±0.08	0.51±0.16	0.22±0.08
Exterior	77	48.8	0.03	30.7	0.76	0.31	16.4	2.69	0.02	0.18	100.2	180.3±5.7	0.22±0.07	4.31±0.34	0.13±0.06	0.29±0.06	0.24±0.17	0.28±0.06
Exterior	81	48.2	0.02	31.0	0.70	0.25	17.5	2.24	0.01	0.20	100.1	168.9±5.5	0.34±0.07	3.41±0.28	0.22±0.06	0.33±0.07	0.04±0.06	0.22±0.06
Exterior	75	50.1	0.02	29.8	0.60	0.26	16.1	2.90	0.03	0.21	100.1	160.8±7.0	0.21±0.06	3.32±0.19	0.22±0.04	0.36±0.05	0.33±0.12	0.26±0.06
Interm.	85	48.3	0.01	31.7	0.65	0.23	18.1	1.79	0.01	0.19	100.9	175.0±2.4	0.21±0.03	2.73±0.12	0.19±0.02	0.38±0.04	0.34±0.07	0.26±0.03
Resorption	81	48.9	0.03	30.6	0.62	0.26	17.5	2.26	0.02	0.20	100.3	171.9±2.3	0.10±0.03	2.91±0.15	0.26±0.03	0.27±0.04	0.32±0.10	0.26±0.04
Interm.	85	48.0	0.04	31.2	0.66	0.24	18.1	1.78	0.02	0.22	100.2	177.9±3.1	0.14±0.03	2.66±0.13	0.17±0.04	0.41±0.05	0.27±0.08	0.28±0.04
Interm.	85	48.0	–	31.3	0.67	0.23	18.3	1.82	–	0.20	100.5	171.8±3.1	0.18±0.03	2.91±0.10	0.13±0.02	0.34±0.03	0.17±0.07	0.39±0.07
Interm.	82	48.7	–	30.8	0.68	0.27	17.7	2.10	0.01	0.20	100.4	172.0±3.7	0.18±0.04	2.82±0.13	0.17±0.03	0.39±0.05	0.31±0.09	0.28±0.05
Interm.	83	48.5	0.01	31.2	0.63	0.26	17.5	1.91	0.02	0.21	100.3	170.9±4.2	0.13±0.03	2.98±0.15	0.16±0.03	0.39±0.05	0.33±0.12	0.22±0.06
Interm.	84	48.5	0.02	30.9	0.64	0.25	18.2	1.99	0.02	0.22	100.6	169.6±2.6	0.25±0.05	2.93±0.21	0.19±0.04	0.57±0.19	0.41±0.14	0.25±0.06
Interm.	85	48.2	0.02	31.2	0.62	0.25	18.2	1.77	0.01	0.19	100.5	170.4±4.4	0.15±0.03	2.88±0.13	0.19±0.04	0.50±0.06	0.22±0.05	0.35±0.06
63R2 phenocrysts P1–P4																		
P1 Core	73	51.5	0.02	29.0	0.81	0.33	14.8	2.94	0.03	0.17	99.6	–	–	–	–	–	–	–
P1 Interm.	76	50.5	0.03	29.7	0.83	0.33	16.0	2.70	0.02	0.17	100.3	236.4±9.1	0.25±0.07	8.57±0.85	0.43±0.11	0.72±0.16	0.17±0.07	0.24±0.09
P1 Interm.	74	51.1	0.03	29.5	0.81	0.30	15.6	3.06	0.04	0.15	100.6	173.3±5.1	0.12±0.04	4.64±0.49	0.14±0.05	0.49±0.07	0.28±0.14	0.10±0.03
P1 Rim	70	52.5	0.07	28.4	0.97	0.35	14.8	3.43	0.20	0.18	100.9	–	–	–	–	–	–	–
P2 Center	77	50.0	0.03	30.0	0.82	0.31	16.3	2.75	0.02	0.16	100.4	177.6±4.0	0.22±0.06	4.87±0.43	0.31±0.05	0.55±0.10	0.09±0.06	0.32±0.07
P3 Core	73	51.1	0.03	29.7	0.95	0.53	14.2	2.90	0.03	0.14	99.6	–	–	–	–	–	–	–

P3 Rim	68	51.9	0.03	28.7	0.97	0.50	13.7	3.57	0.05	0.17	99.6	195.0±11.2	0.29±1.09	5.98±1.09	0.31±0.22	0.74±0.47	0.56±0.44	0.30±0.12
P4 Core	75	50.2	0.03	30.4	0.74	0.29	15.0	2.80	0.05	0.20	99.8	225.9±11.6	0.11±0.06	8.49±1.22	0.31±0.11	0.62±0.20	0.28±0.14	0.33±0.09
P4 Rim	67	52.5	0.03	28.5	0.95	0.40	13.5	3.67	0.05	0.12	99.7	161.7±4.1	0.13±0.04	3.63±0.39	0.33±0.05	0.69±0.23	0.33±0.09	0.20±0.06
64R2-X1 xenolith																		
Exterior	71	51.7	0.03	29.4	0.99	0.28	14.9	3.29	0.03	0.16	100.7	157.1±3.4	0.13±0.04	2.70±0.23	0.22±0.04	0.37±0.05	0.45±0.18	0.35±0.05
Exterior	79	49.9	–	30.5	0.63	0.28	16.2	2.43	0.01	0.16	100.1	169.3±3.2	0.13±0.03	3.04±0.16	0.21±0.04	0.40±0.07	0.24±0.11	0.39±0.05
Interior	80	49.3	0.02	30.5	0.63	0.25	16.2	2.24	0.01	0.18	99.3	165.9±3.1	0.21±0.05	2.90±0.14	0.22±0.04	0.37±0.05	0.53±0.16	0.38±0.06
Interior	84	48.6	0.01	30.4	0.62	0.22	17.2	1.84	0.01	0.17	99.1	181.6±8.1	0.21±0.06	3.10±0.30	0.16±0.04	0.43±0.07	0.08±0.11	0.41±0.08
Interior	82	49.3	0.02	31.0	0.61	0.25	16.9	2.06	0.02	0.18	100.3	168.2±4.2	0.20±0.03	2.66±0.16	0.25±0.04	0.36±0.05	0.28±0.09	0.32±0.05
Interior	82	49.0	0.02	30.7	0.56	0.25	16.6	1.95	0.01	0.18	99.7	161.2±4.1	0.20±0.05	3.23±0.32	0.16±0.03	0.40±0.07	0.19±0.07	0.21±0.05
Interior	82	48.7	0.01	31.5	0.53	0.26	16.6	1.96	0.02	0.17	99.8	162.0±2.7	0.19±0.04	2.48±0.12	0.18±0.03	0.38±0.04	0.39±0.12	0.44±0.06
Interior	82	48.5	0.01	31.1	0.58	0.27	16.5	2.03	0.02	0.20	99.1	168.7±4.9	0.19±0.04	2.77±0.22	0.10±0.02	0.41±0.07	0.32±0.13	0.41±0.09
Resorption	83	48.0	–	31.9	0.57	0.24	16.7	1.93	0.03	0.21	99.5	167.1±4.4	0.30±0.06	2.53±0.16	0.14±0.03	0.38±0.04	0.21±0.08	0.35±0.06
Interior	80	50.0	–	31.0	0.54	0.26	15.6	2.21	0.02	0.17	99.8	155.9±2.2	0.16±0.03	2.45±0.11	0.21±0.03	0.30±0.03	0.49±0.13	0.36±0.07
64R2 phenocrysts P1–P4																		
P1 Core	69	52.6	0.02	29.2	0.53	0.22	14.4	3.61	0.02	0.15	100.6	186.7±4.5	0.17±0.05	4.06±0.27	0.18±0.04	0.40±0.05	0.31±0.09	0.39±0.07
P1 Interm.	78	50.7	0.02	30.2	0.67	0.29	16.3	2.56	–	0.14	100.7	172.6±2.7	0.13±0.05	2.88±0.16	0.10±0.04	0.33±0.06	0.20±0.10	0.18±0.04
P1 Interm.	74	51.5	0.03	29.1	0.67	0.29	15.1	2.99	–	0.15	99.7	170.0±2.9	0.12±0.04	5.38±1.42	0.15±0.03	0.41±0.05	0.17±0.06	0.25±0.05
P1 Rim	67	52.5	0.04	28.3	0.96	0.30	13.9	3.82	0.05	0.14	100.0	162.0±2.7	–	–	–	–	–	–
P2 Core	83	48.8	0.02	31.4	0.66	0.22	16.5	1.84	–	0.15	99.6	195.2±5.3	0.48±0.15	4.91±0.46	0.43±0.06	0.53±0.10	0.48±0.10	0.43±0.10
P2 Rim	72	51.9	0.04	28.7	0.66	0.30	14.9	3.11	0.03	0.14	99.7	–	–	–	–	–	–	–
P2 Rim	79	50.0	0.04	29.8	0.67	0.28	16.2	2.42	0.02	0.13	99.6	–	–	–	–	–	–	–
P4 Core	66	53.2	0.02	27.8	0.50	0.23	13.5	3.83	0.03	0.10	99.2	–	–	–	–	–	–	–
P4 Interm.	79	48.2	0.04	30.3	0.68	0.25	16.1	2.34	0.01	0.18	99.6	167.9±8.6	0.38±0.12	2.63±0.28	0.18±0.06	0.70±0.11	0.85±0.17	0.27±0.09
P4 Interm.	74	51.0	0.04	28.8	0.73	0.30	14.8	3.26	0.03	0.17	99.9	182.7±3.8	0.38±0.15	4.81±0.45	0.32±0.09	0.72±0.08	0.44±0.15	0.21±0.07
P4 Rim	65	52.6	0.06	27.7	1.04	0.26	13.3	3.99	0.03	0.11	99.0	–	–	–	–	–	–	–
P3 Core	78	50.3	0.01	29.8	0.68	0.29	15.8	2.39	0.03	0.13	99.5	183.0±7.5	0.26±0.07	3.27±0.38	0.09±0.06	0.45±0.10	0.14±0.13	0.13±0.07
P3 Interm.	75	51.0	0.03	29.4	0.71	0.29	15.8	2.85	0.02	0.16	100.3	180.9±3.6	0.27±0.08	4.87±0.51	0.38±0.09	0.44±0.10	0.28±0.22	0.34±0.09
807-X1 xenolith																		
Core	83	47.0	–	31.3	0.78	0.26	18.7	2.02	0.18	–	100.2	–	–	–	–	–	–	–
Core	84	47.0	–	31.5	0.65	0.22	18.9	1.88	0.14	–	100.2	–	–	–	–	–	–	–
Core	84	47.2	–	31.3	0.89	0.29	18.6	1.94	0.11	–	100.2	–	–	–	–	–	–	–
Interm.	83	47.4	–	31.3	0.71	0.22	18.6	2.02	0.15	–	100.5	–	–	–	–	–	–	–
Interm.	83	46.6	–	31.5	0.72	0.27	18.9	2.14	0.05	–	100.2	–	–	–	–	–	–	–
Interm.	83	47.1	–	31.3	0.76	0.27	18.9	2.06	0.11	–	100.5	–	–	–	–	–	–	–
Rim	74	49.7	–	28.9	0.68	0.28	16.2	2.99	0.19	–	98.9	–	–	–	–	–	–	–
Rim	71	50.8	–	28.3	0.79	0.32	15.6	3.41	0.16	–	99.3	–	–	–	–	–	–	–
Rim	74	50.1	–	29.1	0.73	0.29	16.0	2.97	0.20	–	99.4	–	–	–	–	–	–	–
Average LA–ICP–MS detection limits																		
12 µm pit	–	–	–	–	–	–	–	–	–	–	–	0.33	0.14	0.10	0.07	0.03	0.05	0.06
25 µm pit	–	–	–	–	–	–	–	–	–	–	–	0.12	0.06	0.07	0.04	0.03	0.03	0.03
NIST 614 measured	–	–	–	–	–	–	–	–	–	–	–	44.7±1.9	0.76±0.06	3.25±0.27	0.73±0.02	0.81±0.1	0.73±0.04	0.73±0.03
NIST 614 recommended	–	–	–	–	–	–	–	–	–	–	–	45.1	0.80	3.13	0.71	0.78	0.75	0.73

Interm.=Intermediate area between core and rim of largest discernable plagioclase crystal in each xenolith.

FeO_T=Fe reported as total FeO.

Major elements in wt.% and trace elements in ppm.

ICP–MS detection limits calculated using methods described in Longerich et al. (1996).

ICP–MS analytical error calculated using methods described in Longerich et al. (1996) and Norman et al. (1996).

NIST 614 values reported are the average of 10 measurements.

Magmatic water can affect D values by decreasing the activity of trace element components in silicate melts (Wood and Blundy, 2002). However, Kwaimbaita basaltic glass samples have relatively low H_2O contents (generally ≤ 0.22 wt.%; Roberge et al., 2004), so we estimate the effect of water on OJP plagioclase D values to be negligible.

The partitioning studies of Bindeman et al. (1998) were run in air such that their equations and constants for calculation of D_{Eu} and D_{Fe} (hereafter D_{FeO_T} for total Fe as FeO) neglect the effects of magma oxygen fugacity (fO_2). Oxygen fugacity affects the partitioning of Fe and Eu in plagioclase (Wilke and Behrens, 1999). Trivalent Fe substitutes for Al^{3+} in the tetrahedral site, Eu^{2+} substitutes in the plagioclase M cation site at low fO_2, and Eu^{3+} present at higher fO_2 is incompatible (Longhi et al., 1976; Smith and Brown, 1988; Deer et al., 2001). We estimated a $D_{Eu} \approx 0.43$ graphically from Blundy (1997; his Fig. 3: D_{Eu} vs. ΔQFM of basaltic magma), where it was demonstrated that D_{Eu} increased systematically with decreasing fO_2 in basalts. We estimate $D_{FeO_T} \approx 0.065$ for OJP plagioclase. This value is an average from experimental crystallization studies of Kwaimbaita basalt by Sano and Yamashita (2004) at the QFM buffer, which is the approximate fO_2 condition of OJP basalt crystallization suggested by Roberge et al. (2004). This estimate of D_{FeO_T} is supported by the results of Phinney (1994) who reported little change in D_{FeO_T} at fO_2 below the QFM oxygen buffer, while D_{FeO_T} increased steadily at higher fO_2, which was attributed to greater amounts of Fe^{3+} in the melt.

If generally constant partitioning of Mg between plagioclase and melt is assumed (i.e., using the method of Bindeman et al., 1998), we calculate an average D_{Mg} value of 0.024 ± 0.005 for the OJP plagioclase crystals considered in this study. The minor variation of D_{Mg}, using the Bindeman et al. (1998) method, over the large compositional range of plagioclase examined in this study (An_{65-86}) is in accordance with Longhi et al. (1976) and Bindeman et al. (1998) who suggested that An content has minimal effect on Mg partitioning. However, the average D_{Mg} values calculated using the equations and constants of Bindeman et al. (1998) are inconsistent with the experimental results of Sano and Yamashita (2004), whose results for OJP basalts reveal slightly larger values for Kwaimbaita (0.1 MPa $D_{Mg}=$ 0.043; 190 MPa $D_{Mg}=0.055$) and Kroenke basalts (0.1 MPa $D_{Mg}=0.04$; 190 MPa $D_{Mg}=0.06$) at elevated pressures. This suggests that crystallization pressure may have an effect on D_{Mg} (Sano and Yamashita, 2004). We use $D_{Mg} \approx 0.047$ to invert parent magma compositions of OJP plagioclase crystals, which is an average of

eight D_{Mg} values from the experimental results of Sano and Yamashita (2004) conducted at 0.1 and 190 MPa. Phinney (1994) reported an average basaltic plagioclase D_{Mg} value of 0.044, which is consistent with our selected D_{Mg} value.

5. Results

5.1. Plagioclase zoning patterns

5.1.1. Malaita xenolith (ML-X1)

Plagioclase cumulate xenoliths from Malaita are round to sub-round, generally 1–8 cm in diameter, consist entirely of interlocking plagioclase crystals, and are generally moderately altered (Fig. 3A–D). Alteration is evident as fracturing and discoloration of xenolith crystals (e.g., Fig 3C). The xenolith we examined from Malaita (ML-X1) is larger than xenoliths from Site 1183 or 807 (6.7 cm diameter, roughly twice the diameter than the largest Site 1183 xenolith from Unit 7). ML-X1 contains zones of small devitrified melt inclusions oriented parallel to oscillatory zoning and is completely altered along its rim (Fig. 3C,E). It also contains small olivine (now completely altered to clay minerals) and clinopyroxene grains along its margins (Fig. 3C). We collected major and trace element data from the least altered interior section of ML-X1, which exhibited oscillatory zonation (Figs. 3B and 6A).

5.1.2. Site 1183 xenoliths

The three rounded xenoliths we examined from Site 1183 are texturally similar, and Mahoney et al. (2001) suggested that they have a cumulate origin (Fig. 2A,B). The Site 1183 xenoliths contain only sparse melt inclusions, are primarily oscillatory zoned, and are 0.5–3 cm in diameter (Mahoney et al., 2001; Fig. 2). There are distinct resorption/reaction rims on each of the crystals that are common to the entire xenolith rather than individual crystals (Fig. 2E,F). We refer to these common rim sections as xenolith exteriors (see Fig. 2E). All three Site 1183 xenoliths contain clinopyroxene and completely altered olivine grains in similar proportions along the xenolith margins (e.g., Fig. 2D,F). Similarly, all three xenoliths contain patches of devitrified glass and minor clinopyroxene that appears to have been almost completely melted out (Mahoney et al., 2001; Fig. 2C). The Site 1183 xenolith crystals we examined contain few resorption features, exceptions are the core region of the Unit 7 xenolith crystal (Fig. 2B) and a small resorption surface in the Unit 6 xenolith (Fig. 2E). Selected major and trace element data
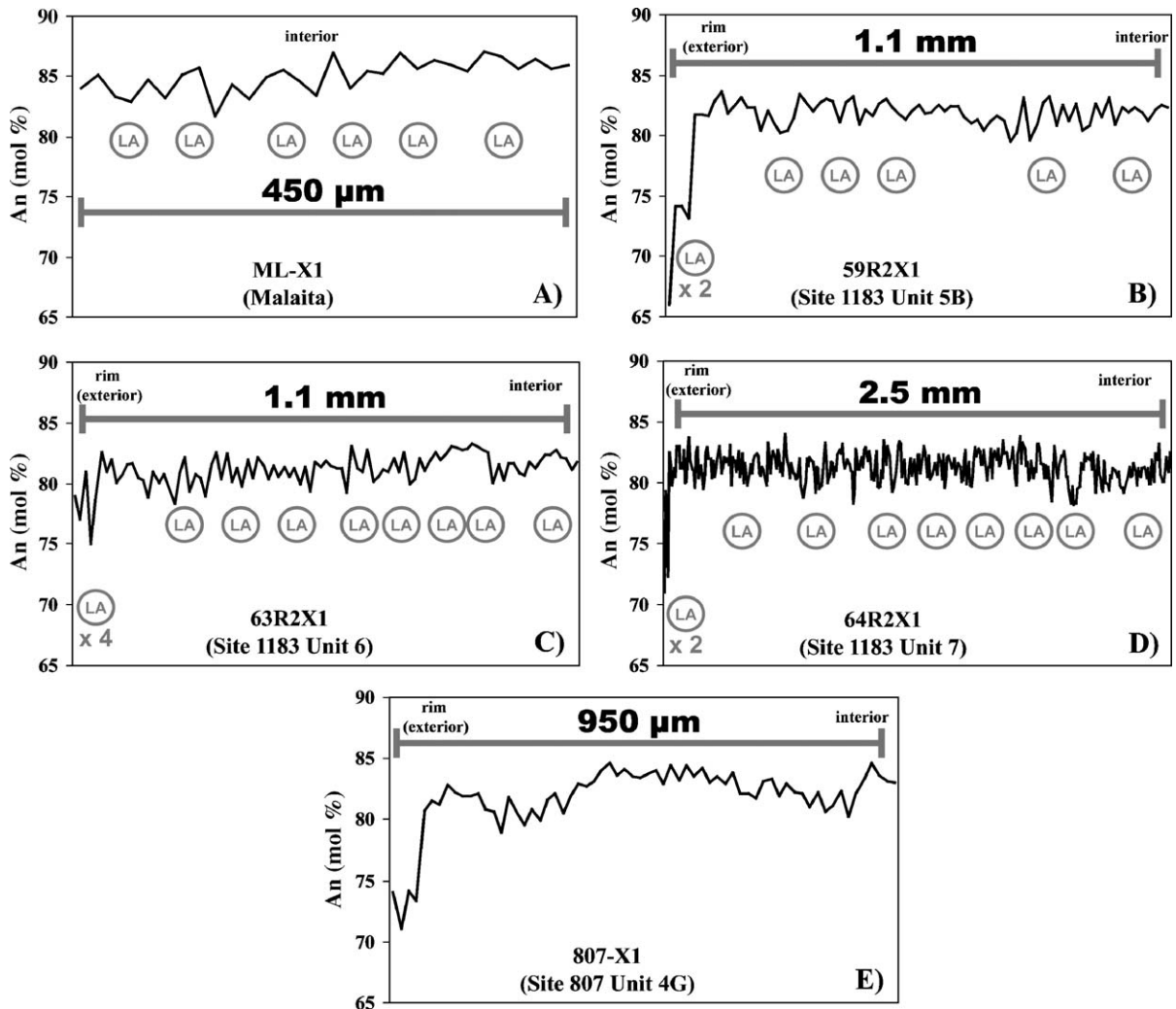
Fig. 6. Major and trace element data were collected along a traverse from interior to rim (i.e., exterior). Locations LA–ICP–MS analysis sites are illustrated (labeled LA) along the measured core to rim An profile of each plagioclase crystal: (A) interior section of xenolith crystal ML-X1, Malaita; (B) xenolith crystal 59R2-X1, ODP Site 1183 Unit 5B (192-1183A-59R2 112–117 cm piece #10A); (C) xenolith crystal 63R2-X1, ODP Site 1183 Unit 6 (192-1183A-63R2 25–27 cm piece #4); (D) xenolith crystal 64R2-X1, ODP Site 1183 Unit 7 (192-1183A-64R2 116–120 cm piece #9B); (E) xenolith crystal 807-X1, ODP Site 807 (130-807C-93R-1-137-139).

collected along core to rim transects in each crystal are displayed in Table 2 (see also Fig. 6B–D).

5.1.3. Site 1183 phenocrysts

Sano and Yamashita (2004) documented two types of zoned plagioclase phenocrysts, Types I and II, in Kwaimbaita basalts from Site 1183 and other ODP drill sites. Type I crystals are generally euhedral, exhibit normal zonation, and have An_{73} to An_{78} cores (e.g., Fig. 5A). Type II crystals have complex zoning, exhibit reverse or oscillatory zonations, and have cores in the An_{73} to An_{78} range that are commonly surrounded by An_{80} to An_{84} zones (Sano and Yamashita, 2004; e.g.,

Fig. 5B). Representative examples of the different zoning types are shown in Fig. 5. We observed similar zoning patterns in the Units 5B, 6, and 7 Kwaimbaita basalts from Site 1183. Basalts from Units 5B and 6 contain primarily Type I normal zoned phenocrysts, whereas the Unit 7 basalt we examined contains a mixture of Type I normal and Type II reverse zoned phenocrysts (Table 1). Plagioclase phenocrysts from Unit 7 exhibit other morphological differences from Units 5B and 6 phenocrysts. For example, 64R2-P3 from Unit 7 is part of a plagioclase–olivine glomerocryst and has a sieve textured core (Fig. 5C). Olivine was entirely replaced with clay minerals and was

Table 2
Calculated partition coefficients and equilibrium liquid compositions

Crystal zone	An (mol%)	D_{Sr}	D_{Ti}	D_Y	D_{Ba}	D_{La}	D_{Ce}	D_{Nd}	D_{Eu}	D_{Mg}	D_{Fe}	Sr	Ti	Y	Ba	La	Ce	Nd	Eu	Mg#	Ba/Sr	La/Y	Sr/Ti
ML-X1 xenolith																							
Interior	85	1.26	0.04	0.03	0.10	0.17	0.11	0.12	0.43	0.047	0.065	136.8	3331	8.00	22.08	1.41	5.52	–	0.58	0.30	0.16	0.18	0.04
Interior	85	1.24	0.04	0.03	0.10	0.17	0.10	0.11	0.43	0.047	0.065	130.5	1991	7.05	29.68	0.99	2.37	3.30	0.78	0.31	0.23	0.14	0.07
Interior	85	1.24	0.04	0.03	0.10	0.17	0.11	0.11	0.43	0.047	0.065	142.1	3664	7.51	18.91	1.19	3.49	3.39	0.81	0.32	0.13	0.16	0.04
Interior	86	1.23	0.04	0.03	0.10	0.17	0.10	0.11	0.43	0.047	0.065	152.3	2036	5.15	21.85	1.52	3.49	6.71	0.97	0.31	0.14	0.26	0.07
Interior	84	1.28	0.04	0.03	0.11	0.17	0.11	0.12	0.43	0.047	0.065	135.0	2147	–	27.01	2.32	3.40	3.29	1.10	0.33	0.20	–	0.06
Interior	86	1.21	0.04	0.02	0.10	0.17	0.10	0.11	0.43	0.047	0.065	153.6	4392	17.51	32.31	1.81	5.25	2.03	–	0.31	0.21	0.10	0.03
59R2-X1 xenolith																							
Exterior	66	1.99	0.06	0.06	0.24	0.20	0.14	0.16	0.43	0.047	0.065	–	2998	–	–	–	–	–	0.18	–	–	–	–
Exterior	75	1.61	0.05	0.04	0.16	0.19	0.12	0.14	0.43	0.047	0.065	140.6	9313	4.76	30.42	2.33	5.26	3.60	1.13	0.32	0.22	0.49	0.02
Interior	81	1.39	0.04	0.03	0.13	0.18	0.11	0.12	0.43	0.047	0.065	–	5985	–	–	–	–	–	0.30	–	–	–	–
Interior	82	1.35	0.04	0.03	0.12	0.17	0.11	0.12	0.43	0.047	0.065	148.2	7881	4.55	32.29	1.56	4.26	2.51	1.04	0.30	0.22	0.34	0.02
Interior	83	1.30	0.04	0.03	0.11	0.17	0.11	0.12	0.43	0.047	0.065	168.5	3953	6.58	41.83	1.29	5.20	4.38	1.05	0.29	0.25	0.20	0.04
Interior	82	1.33	0.04	0.03	0.12	0.17	0.11	0.12	0.43	0.047	0.065	152.6	2929	4.17	31.19	1.15	5.48	3.50	1.09	0.31	0.20	0.28	0.05
Center/core	83	1.30	0.04	0.03	0.11	0.17	0.11	0.12	0.43	0.047	0.065	158.5	2461	6.79	45.33	1.79	5.36	5.42	0.79	0.29	0.29	0.26	0.06
59R2-P1 phenocryst																							
P1 rim	71	1.76	0.05	0.05	0.19	0.19	0.13	0.14	0.43	0.047	0.065	115.0	5117	6.45	31.46	1.81	5.44	5.38	0.89	0.30	0.27	0.28	0.02
P1 core	74	1.63	0.05	0.04	0.17	0.19	0.12	0.14	0.43	0.047	0.065	114.8	6525	3.22	25.56	1.92	4.35	3.04	0.99	0.29	0.22	0.60	0.02
P2 rim	70	1.79	0.05	0.05	0.20	0.19	0.13	0.15	0.43	0.047	0.065	115.4	8039	4.79	26.36	2.01	5.40	3.13	1.09	0.30	0.23	0.42	0.01
P2 core	73	1.68	0.05	0.04	0.18	0.19	0.13	0.14	0.43	0.047	0.065	116.6	5962	8.20	25.85	2.42	4.14	3.35	0.90	0.33	0.22	0.30	0.02
P3 center	69	1.84	0.05	0.05	0.21	0.20	0.13	0.15	0.43	0.047	0.065	–	3597	–	–	–	–	–	0.30	–	–	–	–
P4 center	67	1.97	0.06	0.05	0.24	0.20	0.14	0.16	0.43	0.047	0.065	–	2998	–	–	–	–	–	0.31	–	–	–	–
63R2-X1 xenolith																							
Exterior	79	1.40	0.04	0.03	0.13	0.18	0.11	0.12	0.43	0.047	0.065	127.9	7685	8.64	24.02	1.14	3.83	4.14	0.52	0.29	0.19	0.13	0.02
Exterior	77	1.51	0.05	0.04	0.15	0.18	0.12	0.13	0.43	0.047	0.065	119.4	6671	6.28	29.48	0.71	2.47	1.83	0.65	0.31	0.25	0.11	0.02
Exterior	81	1.37	0.04	0.03	0.12	0.18	0.11	0.12	0.43	0.047	0.065	123.3	5807	11.18	27.88	1.29	2.94	0.33	0.50	0.28	0.23	0.11	0.02
Exterior	75	1.63	0.05	0.04	0.17	0.19	0.12	0.14	0.43	0.047	0.065	101.1	5033	5.39	20.65	1.20	2.91	2.47	0.62	0.32	0.20	0.24	0.02
Interm.	85	1.25	0.04	0.03	0.10	0.17	0.11	0.12	0.43	0.047	0.065	138.0	1435	7.41	25.45	1.08	3.24	2.58	0.61	0.27	0.18	0.15	0.10
Resorption	81	1.38	0.04	0.03	0.12	0.18	0.11	0.12	0.43	0.047	0.065	124.9	6266	3.27	23.56	1.46	2.39	2.64	0.61	0.31	0.19	0.45	0.02
Interm.	85	1.25	0.04	0.03	0.10	0.17	0.11	0.12	0.43	0.047	0.065	142.3	9791	5.43	25.59	1.00	3.89	2.38	0.65	0.29	0.18	0.18	0.01
Interm.	85	1.25	0.04	0.03	0.10	0.17	0.11	0.12	0.43	0.047	0.065	137.0	–	6.79	27.84	0.78	3.15	1.45	0.90	0.27	0.20	0.12	–
Interm.	82	1.33	0.04	0.03	0.12	0.17	0.11	0.12	0.43	0.047	0.065	129.3	–	6.11	24.27	1.01	3.52	2.58	0.65	0.30	0.19	0.16	–
Interm.	83	1.29	0.04	0.03	0.11	0.17	0.11	0.12	0.43	0.047	0.065	132.2	3055	4.78	27.06	0.95	3.60	2.80	0.52	0.30	0.20	0.20	0.04
Interm.	84	1.27	0.04	0.03	0.11	0.17	0.11	0.12	0.43	0.047	0.065	133.5	4651	9.05	27.45	1.11	5.34	3.56	0.57	0.30	0.21	0.12	0.03
Interm.	85	1.24	0.04	0.03	0.10	0.17	0.11	0.11	0.43	0.047	0.065	137.0	4422	5.76	27.93	1.10	4.70	1.92	0.82	0.30	0.20	0.19	0.03
63R2-P1 phenocryst																							
P1 Interm.	76	1.54	0.05	0.04	0.15	0.18	0.12	0.13	0.43	0.047	0.065	153.6	6571	6.69	56.62	2.36	5.97	1.31	0.57	0.30	0.37	0.35	0.02
P1 Interm.	74	1.65	0.05	0.04	0.17	0.19	0.12	0.14	0.43	0.047	0.065	105.0	5171	3.02	27.06	0.73	3.96	2.03	0.23	0.28	0.26	0.24	0.02

P2 center	77	1.54	0.05	0.04	0.15	0.18	0.12	0.13	0.43	0.047	0.065	115.5	5876	6.09	32.24	1.68	4.59	0.67	0.75	0.29	0.28	0.28	0.02
P3 cim	68	1.91	0.06	0.05	0.22	0.20	0.14	0.15	0.43	0.047	0.065	102.0	4513	5.58	26.69	1.55	5.47	3.67	0.70	0.36	0.26	0.28	0.02
P4 core	75	1.62	0.05	0.04	0.17	0.19	0.12	0.14	0.43	0.047	0.065	139.8	5920	2.71	51.41	1.64	5.03	2.09	0.76	0.29	0.37	0.61	0.02
P4 rim	67	1.96	0.06	0.05	0.23	0.20	0.14	0.15	0.43	0.047	0.065	82.7	4345	2.41	15.57	1.64	5.02	2.15	0.46	0.31	0.19	0.68	0.02
64R2-X1 xenolith																							
Rim	71	1.76	0.05	0.05	0.19	0.19	0.13	0.14	0.43	0.047	0.065	89.5	6605	2.96	14.05	1.16	2.82	3.09	0.83	0.23	0.16	0.39	0.01
Rim	79	1.46	0.04	0.03	0.14	0.18	0.12	0.13	0.43	0.047	0.065	115.9	757	3.75	22.06	1.18	3.47	1.91	0.91	0.32	0.19	0.31	0.15
Interior	80	1.51	0.04	0.03	0.13	0.18	0.11	0.12	0.43	0.047	0.065	117.4	4832	6.43	22.41	1.23	3.23	4.23	0.87	0.30	0.19	0.19	0.02
Interior	84	1.29	0.04	0.03	0.11	0.17	0.11	0.12	0.43	0.047	0.065	141.2	3288	7.72	28.37	0.92	3.93	0.68	0.96	0.28	0.20	0.12	0.04
Interior	82	1.35	0.04	0.03	0.12	0.17	0.11	0.12	0.43	0.047	0.065	124.9	5056	6.62	22.40	1.41	3.26	2.31	0.73	0.31	0.18	0.21	0.02
Interior	82	1.34	0.04	0.03	0.12	0.17	0.11	0.12	0.43	0.047	0.065	120.2	5862	6.90	27.39	0.92	3.64	1.57	0.48	0.29	0.23	0.13	0.02
Interior	82	1.33	0.04	0.03	0.12	0.17	0.11	0.12	0.43	0.047	0.065	121.6	3332	6.61	21.33	1.03	3.47	3.21	1.03	0.34	0.18	0.16	0.04
Interior	82	1.35	0.04	0.03	0.12	0.17	0.11	0.12	0.43	0.047	0.065	124.7	3900	6.41	23.10	0.58	3.64	2.63	0.94	0.33	0.19	0.09	0.03
Interior	83	1.32	0.04	0.03	0.12	0.17	0.11	0.12	0.43	0.047	0.065	126.2	–	10.22	22.00	0.83	3.43	1.76	0.81	0.31	0.17	0.08	–
Interior	80	1.43	0.04	0.03	0.13	0.18	0.11	0.13	0.43	0.047	0.065	109.2	–	4.83	18.55	1.15	2.60	3.88	0.83	0.34	0.17	0.24	–
64R2-P1 phenocryst																							
P1 Core	69	1.87	0.06	0.05	0.21	0.20	0.13	0.15	0.43	0.047	0.065	100.0	4378	3.35	18.91	0.90	2.99	2.05	0.91	0.31	0.19	0.27	0.02
P1 Interm.	78	1.49	0.05	0.03	0.14	0.18	0.12	0.13	0.43	0.047	0.065	115.9	4822	3.73	20.18	0.57	2.80	1.58	0.41	0.32	0.17	0.15	0.02
P1 Interm.	74	1.66	0.04	0.04	0.17	0.19	0.13	0.14	0.43	0.047	0.065	102.6	6897	2.87	31.09	0.79	3.24	1.19	0.59	0.32	0.30	0.29	0.01
P2 Core	83	1.30	0.04	0.03	0.11	0.17	0.11	0.12	0.43	0.047	0.065	150.1	4125	17.18	44.03	2.50	4.87	4.03	0.99	0.26	0.29	0.15	0.04
P2 Rim	72	1.70	0.05	0.04	0.18	0.19	0.13	0.14	0.43	0.047	0.065	–	5216	–	–	–	–	–	–	0.31	–	–	–
P4 Interm.	79	1.44	0.04	0.03	0.13	0.18	0.12	0.13	0.43	0.047	0.065	116.5	8180	11.37	19.58	1.00	6.04	6.75	0.62	0.28	0.17	0.09	0.01
P4 Interm.	74	1.66	0.05	0.04	0.17	0.19	0.13	0.14	0.43	0.047	0.065	110.2	7640	9.09	27.82	1.68	5.77	3.20	0.50	0.31	0.25	0.18	0.01
P3 Core	78	1.47	0.04	0.03	0.14	0.18	0.12	0.13	0.43	0.047	0.065	124.7	1576	7.51	23.57	0.50	3.89	1.10	0.31	0.31	0.19	0.07	0.08
P3 Interm.	75	1.58	0.05	0.04	0.16	0.18	0.12	0.13	0.43	0.047	0.065	114.2	6477	7.05	30.56	2.07	3.62	2.11	0.80	0.30	0.27	0.29	0.02
807-X1 xenolith																							
Core	83	–	–	–	–	–	–	–	–	0.047	0.065	–	–	–	–	–	–	–	–	0.26	–	–	–
Core	84	–	–	–	–	–	–	–	–	0.047	0.065	–	–	–	–	–	–	–	–	0.27	–	–	–
Core	84	–	–	–	–	–	–	–	–	0.047	0.065	–	–	–	–	–	–	–	–	0.26	–	–	–
Interm.	83	–	–	–	–	–	–	–	–	0.047	0.065	–	–	–	–	–	–	–	–	0.25	–	–	–
Interm.	83	–	–	–	–	–	–	–	–	0.047	0.065	–	–	–	–	–	–	–	–	0.29	–	–	–
Interm.	83	–	–	–	–	–	–	–	–	0.047	0.065	–	–	–	–	–	–	–	–	0.28	–	–	–
Rim	74	–	–	–	–	–	–	–	–	0.047	0.065	–	–	–	–	–	–	–	–	0.30	–	–	–
Rim	71	–	–	–	–	–	–	–	–	0.047	0.065	–	–	–	–	–	–	–	–	0.30	–	–	–
Rim	74	–	–	–	–	–	–	–	–	0.047	0.065	–	–	–	–	–	–	–	–	0.29	–	–	–

Interm. = Intermediate area between core and rim of largest discernable plagioclase crystal in each xenolith.

FeO_T = Fe reported as total FeO.

Major elements in wt.% and trace elements including Ti in ppm.

Mg# = [Mg/(Mg+Fe)].

identified by its morphology. Melt inclusions are more abundant in phenocrysts from Unit 7 relative to Units 5B and 6 (e.g., 64R2-P1; Fig. 5D). Unit 7 basalts also contain plagioclase–clinopyroxene glomerocrysts and partially resorbed strained clinopyroxene xenocrysts (Mahoney et al., 2001).
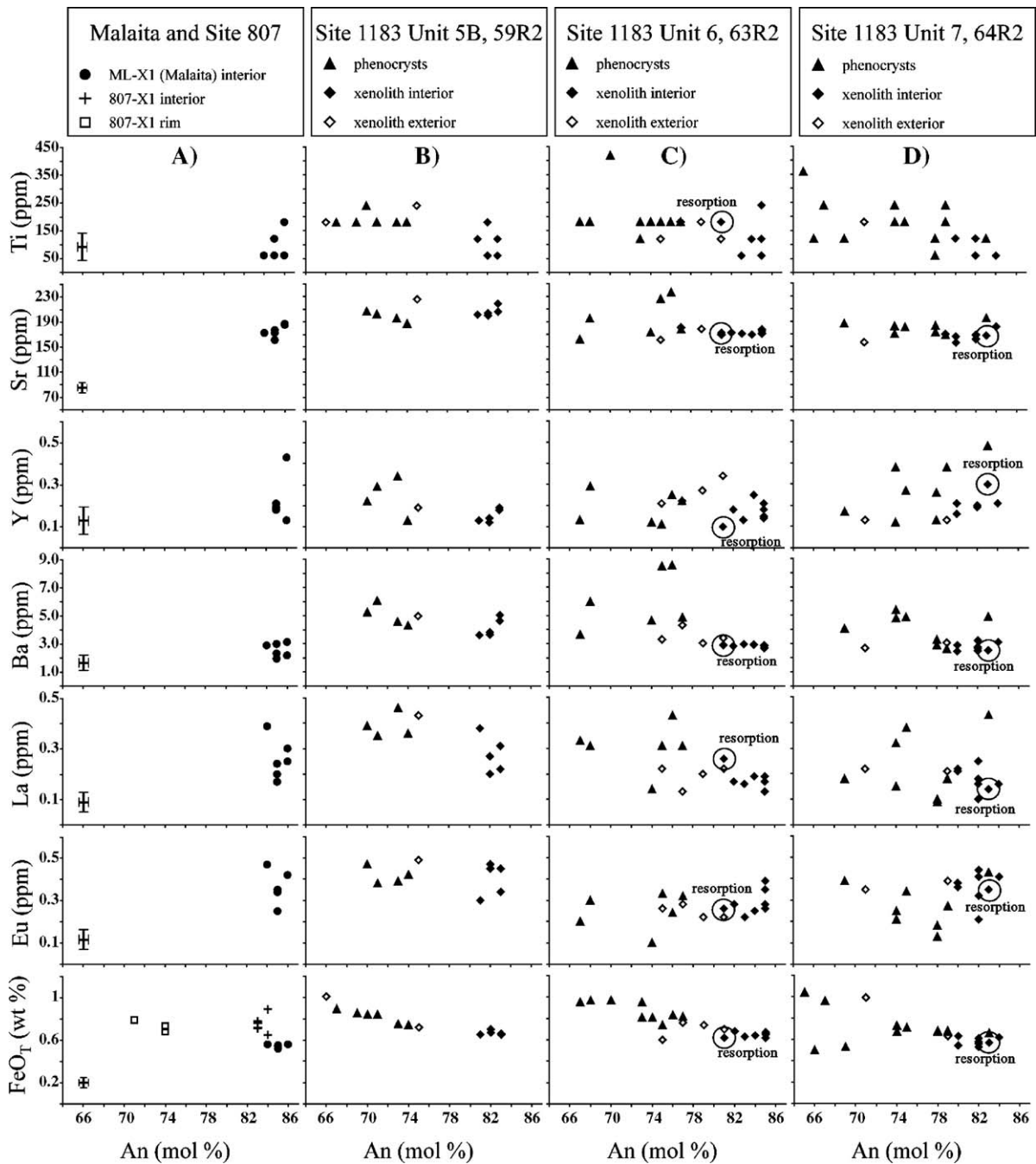

Fig. 7. Measured major and trace element data vs. An content of xenolith plagioclase crystals and plagioclase phenocrysts from: (A) ML-X1 (Malaita) and 807-X1 (130-807C-93R-1-137-139); (B) ODP Site 1183 Unit 5B xenolith 59R2-X1 (192-1183A-59R2 112–117 cm piece #10A); (C) ODP Site 1183 Unit 6 xenolith 63R2-X1 (192-1183A-63R2 25–27 cm piece #4); (D) ODP Site 1183 Unit 7 xenolith 64R2-X1 (192-1183A-64R2 116–120 cm piece #9B). Resorption features examined in the Unit 6 and Unit 7 xenolith crystals are noted in columns C and D. Average analytical uncertainties (analytical precision relative 1σ) calculated for each segment of signal integrated for each element are displayed as error bars in column A. Ti and FeO$_T$ measured by EPMA, all others measured by LA–ICP–MS.

5.1.4. Site 807 xenolith (807-X1)

Plagioclase xenoliths, although smaller and commonly in the form of glomerocrysts, were noted in Kwaimbaita basalts from ODP Site 807 (Mahoney et al., 1993a,b). The sub-round xenolith we examined from the Site 807 (807-X1) has a similar morphology to the larger xenoliths from Site 1183 and Malaita but is more disaggregated (Fig. 3E). Xenolith 807-X1 is composed primarily of interlocking plagioclase grains and contains small clinopyroxene and completely altered olivine grains in similar proportions along its margins (130-807C-93R-1-137-139; Unit 4G; 1525.8 mbsf; Kroenke et al., 1991; Fig. 3E,F). Major and minor element data only are reported in Table 1 for selected points sampled along a transect from the core area to the rim of a single large xenolith crystal (Fig. 6E).

5.2. Measured compositions

5.2.1. Major elements

The interior sections of xenolith crystals have greater An content (An_{80}–An_{86}) than the xenolith exteriors and phenocrysts, which display a similar range of An content (An_{65}–An_{83}) (see Table 1 and Figs. 7 and 8). Phenocrysts from Site 1183 Units 5B, 6, and 7 trend to lower An (An_{65-73}) content than phenocrysts reported by Sano and Yamashita (2004) (An_{73-78}) (Table 1). The phenocrysts contain FeO_T, MgO, and Ti within the ranges exhibited by xenolith interiors, but do however extend to higher abundances of these elements (see Table 1). In Table 1, we display representative major and trace element data of both xenolith crystals and phenocrysts. Note that Ti was measured by EPMA. A

spreadsheet of all major element data is available in an online archive (see Supplementary data).

5.2.2. Trace elements

Selected trace element abundances measured in xenolith crystals and phenocrysts are plotted against mol% An of plagioclase in Fig. 7 for samples from Malaita, Site 1183, and Site 807. With the exception of Eu, a general negative correlation of element concentration with An content is apparent, which is a likely result of the greater ease of trace element partitioning into the more elastic structure of the relatively albite-rich plagioclase (e.g., Blundy and Wood, 1991; Fig. 7). Phenocrysts contain concentrations of La, Ce, and Nd that overlap the ranges exhibited by xenolith interiors, but extend to higher abundances (see Table 1). Xenolith crystals and phenocrysts contain similar Y and Eu abundances (Fig. 7).

5.3. Parental magma compositions

5.3.1. Major elements

Parent magmas of the An-rich xenolith interiors tend to have lower Ti at a given Mg number (Mg/[Mg+Fe]) than phenocryst parent magmas. On a plot of Mg number vs. Ti, phenocryst parent magmas overlap the Kwaimbaita whole-rock basalt field, whereas the An-rich xenolith interiors trend below the fields defined by OJP basalts (Fig. 9A; Table 3).

5.3.2. Trace elements

It is difficult to accurately quantify the amount of error introduced by chosen or calculated partition coefficients. Error bars displayed in Figs. 9 and 10, which can be compared to analytical uncertainty displayed in Fig. 7, represent the combined potential error related to analytical uncertainty and calculation of partition coefficients using uncertainty on constants reported by Bindeman et al. (1998). Parent magmas of xenolith interiors typically exhibit lower La/Y and Ba/Sr ratios and slightly higher Sr/Ti ratios than phenocryst parent magmas (Tables 2 and 3; Fig. 9). Parent magmas of the An-rich xenolith interiors are also enriched in Sr, Eu, and Y and relatively depleted in Ba, La, Ce, and Nd relative to phenocryst parent magmas (Tables 2 and 3; Fig. 10). Parent magmas of both xenolith crystals and phenocrysts have Sr, Ba, and Eu abundances that overlap published Kwaimbaita and Kroenke basalt whole-rock values, but generally have lower La, Ce, and Nd abundances (see Table 3). Given the potential error in calculated D values (compare error bars in Figs. 7 and 10), OJP plagioclase parent magmas plot in a

Fig. 8. Measured MgO (wt.%) abundance vs. An content of all xenolith plagioclase crystals and plagioclase phenocrysts examined in this study. All data were obtained by EPMA. Magnesium partitioning is weakly affected or unaffected by plagioclase composition (e.g., Bindeman et al., 1998). We suggest low-pressure (depth range shallower than 7 km) crystallization of relatively primitive OJP magmas can generate low MgO, An-rich plagioclase.
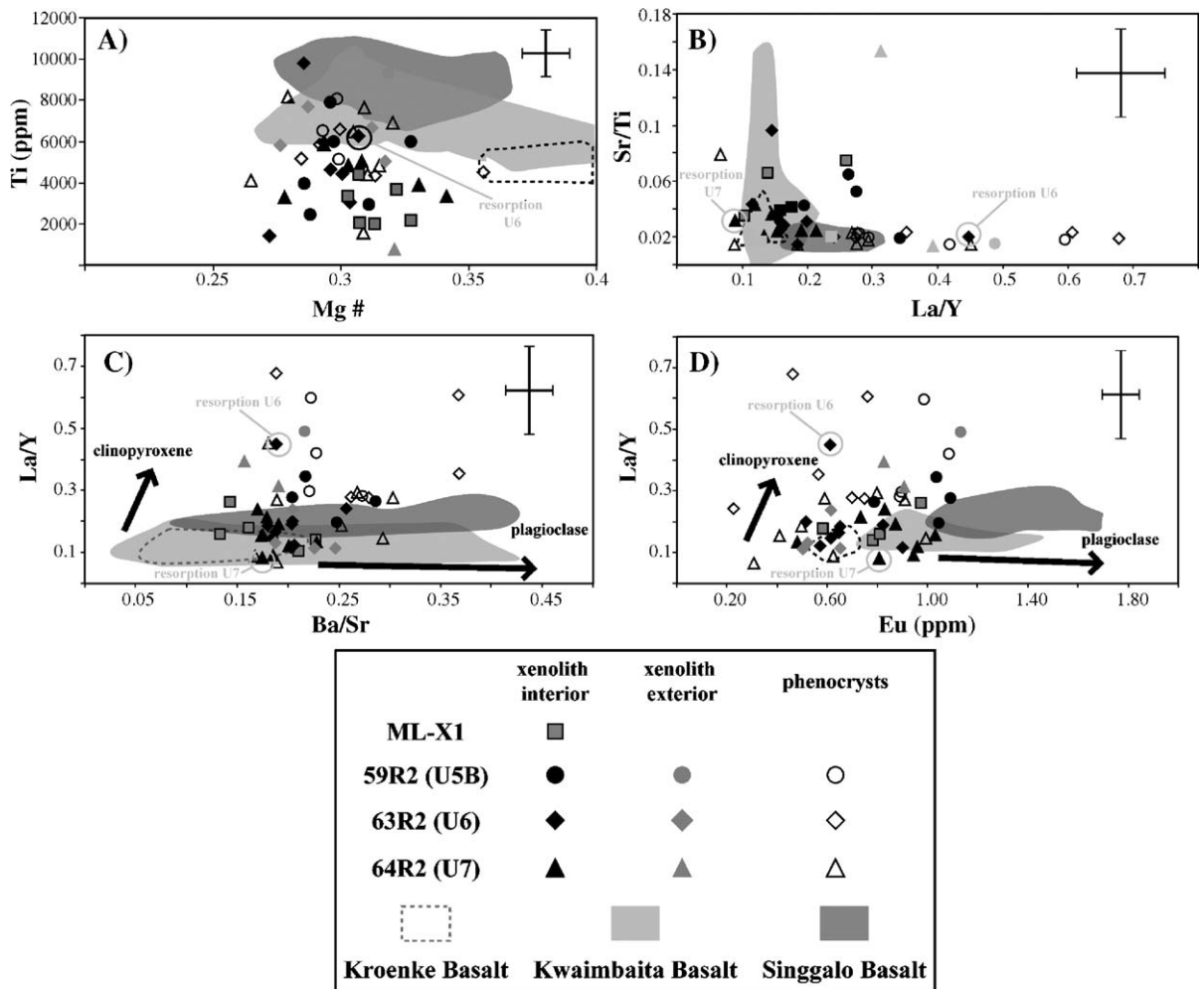
Fig. 9. Trace element ratio plots for parent magmas of OJP plagioclase phenocrysts and xenolith plagioclase crystals. Error bars represent the total potential error obtained by combining the uncertainty of LA–ICP–MS measurements and that inherent in calculating the partition coefficients (D) using uncertainties reported in Bindeman et al. (1998) using standard error propagation. Fields defined by published OJP whole-rock basalt data are displayed (Tejada et al., 2002; Fitton and Goddard, 2004). (A) Ti vs. Mg# [Mg+(Mg+Fe)] data show no distinct differences between xenolith crystals and phenocrysts, except that An-rich crystals tend to have lower Ti and trend to greater Mg#. (B) Sr/Ti vs. La/Y: note phenocryst parent magmas extend to higher La/Y ratios than higher An xenolith crystals. (C) La/Y vs. Ba/Sr: vectors defined by clinopyroxene and plagioclase crystallization of relatively primitive Kroenke basalt are shown as labeled arrows. For illustrative purposes, the head of the arrow on the clinopyroxene vector corresponds to a crystallinity of ∼70%. (D) La/Y vs. Eu and vectors defined by clinopyroxene and plagioclase crystallization of relatively primitive Kroenke basalt. Again, the head of the arrow on the clinopyroxene vector corresponds to a crystallinity of ∼70%. Parent magmas of xenolith crystals and phenocrysts from Site 1183 Unit 7 extend to lower Eu and La/Y.

reasonably consistent manner in terms of La/Y, Sr/Ti, and Ba/Sr ratios, Mg number, Eu and Sr, compared to the Kroenke, Kwaimbaita, and Singgalo whole-rock basalt fields (Fig. 9; Table 3). For example, the compositions of parent magmas of xenolith interiors from Malaita and Unit 7 of Site 1183 overlap Kroenke and Kwaimbaita basalt fields (see Fig. 9). Parent magma compositions of xenolith exteriors and phenocrysts from all three Site 1183 Units and xenolith interior parent magmas from Units 5B and 6 consistently trend outside

of the fields defined by the whole-rock compositions (Fig. 9). Parent magmas of the core and rim of phenocryst 63R2-P4, the core of 59R2-P1, the rim of 59R2-P2, and an exterior zone of xenolith 59R2-X1 are unique, because they have much higher La/Y ratios than whole-rock data or parent magmas of all other xenolith and phenocryst zones examined (see Figs. 9 and 10). A zone within the Unit 6 xenolith associated with a resorption feature has a similarly evolved parent magma and is described in the section that follows.

Table 3
Ranges of major and trace elements in plagioclase, whole-rock data, and calculated parent

Sample	An (mol%)	FeO$_T$	MgO	Ti	Sr	Y	Ba	La	Ce	Nd	Eu	Mg#	Ba/Sr	La/Y	Sr/Ti
Ranges in published whole-rock and glass data															
Kroenke	–	8.9–10.1	7.1–13.6	3410–5790	70.7–194.3	16.1–18.8	4.65–25.63	1.84–2.48	5.19–5.98	4.31–5.23	0.59–0.69	0.36–0.53	0.05–0.29	0.11–0.15	0.02–0.04
Kwaimbaita	–	8.6–12.5	5.3–10.7	4760–10198	33.4–939.3	19.9–37.1	6.97–36.27	2.44–5.19	6.66–13.69	5.58–10.98	0.73–1.34	0.29–0.44	0.03–0.39	0.12–0.19	0.01–0.15
Singgalo	–	10.7–13.5	6.3–8.1	6775–10611	116.4–207.1	18.3–31.8	15.6–133.0	4.06–6.76	11.0–19.6	8.14–14.10	1.02–1.65	0.27–0.36	0.11–1.14	0.18–0.29	0.01–0.02
Ranges measured in OJP plagioclase crystals															
Xenolith Int.	80–86	0.52–0.89	0.22–0.29	0–221	155.9–218.7	0.10–0.43	1.93–5.05	0.10–0.39	0.25–0.63	0.08–0.76	0.21–0.47	–	–	–	–
Xenolith Ext.	66–81	0.60–1.01	0.21–0.32	0–266	157.1–225.7	0.13–0.34	2.70–4.97	0.13–0.43	0.29–0.65	0.05–0.51	0.22–0.49	–	–	–	–
Phenocrysts	65–83	0.50–1.04	0.22–0.53	41–441	161.7–236.4	0.11–0.48	2.63–8.57	0.09–0.46	0.28–0.74	0.09–0.85	0.10–0.47	–	–	–	–
Ranges in parent magmas calculated from OJP plagioclase crystals															
Xenolith Int.	–	8.0–13.7	4.7–6.1	0–9790	109.2–168.5	3.27–17.51	18.55–45.33	0.58–2.32	2.37–5.53	0.68–6.71	0.48–1.10	0.25–0.34	0.13–0.29	0–0.53	0.01–0.10
Xenolith Ext.	–	9.2–15.5	4.4–6.8	0–9313	89.5–140.6	2.96–11.18	14.05–30.42	0.71–2.33	2.47–5.26	0.33–4.14	0.50–1.13	0.23–0.32	0.16–0.25	0.11–0.49	0.01–0.15
Phenocrysts	–	7.7–16.0	4.7–11.3	1576–8180	82.7–153.6	2.41–17.8	15.57–56.62	0.50–2.50	2.19–6.04	0.60–6.75	0–1.09	0.21–0.38	0.17–0.37	0.07–0.68	0.01–0.08

Int.=interior.

Ext.=exterior.

FeOT=Fe reported as total FeO.

Major elements in wt.% and trace elements including Ti in ppm.

Kwaimbaita, Kroenke, and Singgalo whole-rock and glass major and trace element abundances taken from Tejada et al. (2002) and Fitton and Goddard (2004).

Values entered as 0 were below detection limits.

Mg#=[Mg/(Mg+Fe)].
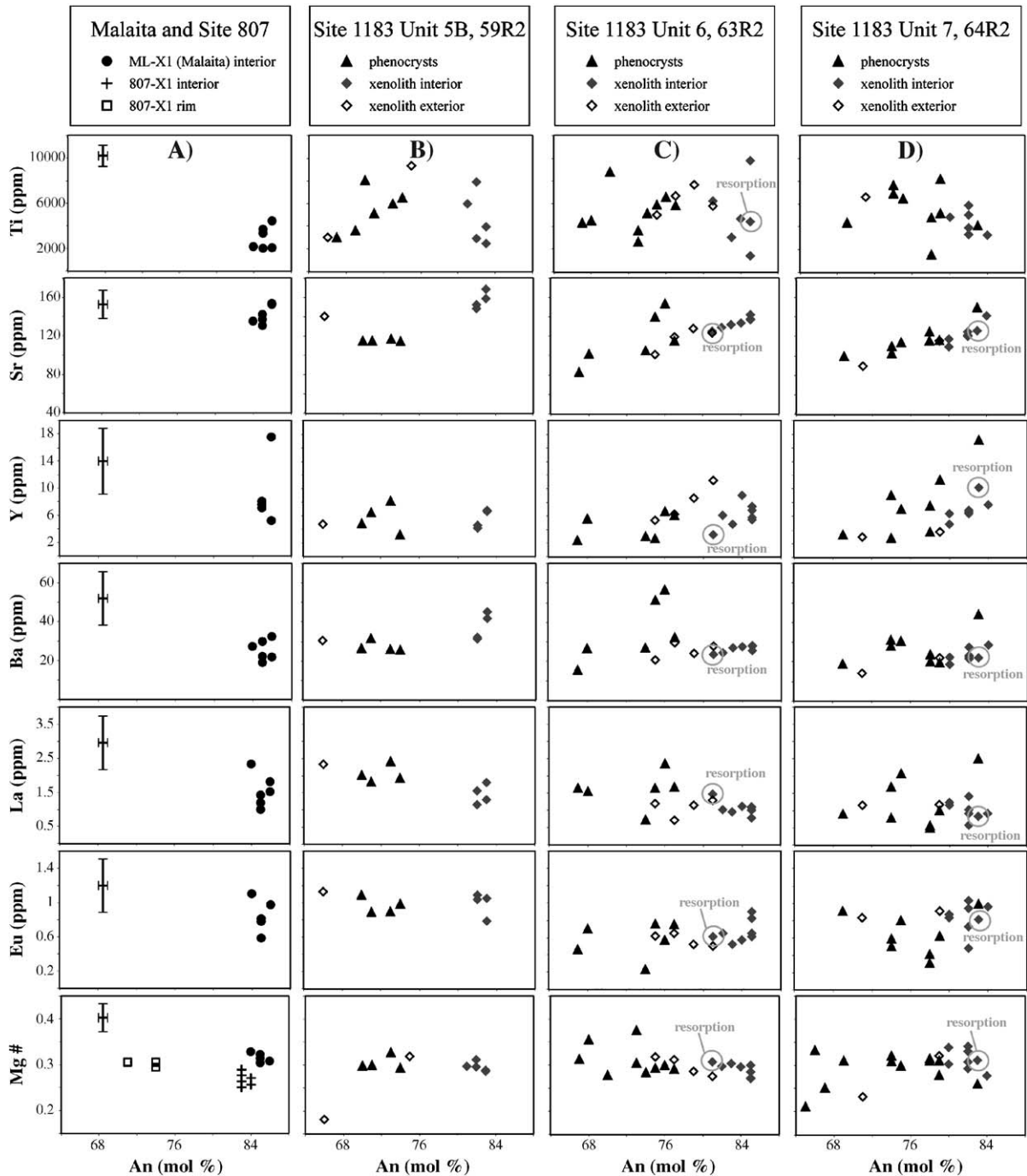
Fig. 10. Calculated major and trace element abundances of magmas that were parental to the studied plagioclase crystals plotted against the An content of each crystal from: (A) ML-X1 (Malaita) and 807-X1 (130-807C-93R-1-137-139); (B) ODP Site 1183 Unit 5B xenolith 59R2-X1 (192-1183A-59R2 112–117 cm piece #10A); (C) ODP Site 1183 Unit 6 xenolith 63R2-X1 (192-1183A-63R2 25–27 cm piece #4); (D) ODP Site 1183 Unit 7 xenolith 64R2-X1 (192-1183A-64R2 116–120 cm piece #9B). Resorption features examined in the Unit 6 and Unit 7 xenolith crystals are noted in columns C and D. The parent magma associated with the resorption feature in the Unit 6 xenolith crystal has the lower Y and Sr, and greater LREE abundance than other parent magma recorded in the same crystal. These data suggest that the zone grown following resorption was in contact with relatively evolved melt. The parent magma of the Unit 7 resorption zone shows the opposite relation ship and appears to relatively primitive. Error bars for the y-axis represent the total potential error obtained by combining the uncertainty of LA–ICP–MS measurements and that inherent in calculating the partition coefficients (D) using uncertainties reported in Bindeman et al. (1998) using standard error propagation. Error bars for the x-axis represent analytical uncertainty.

5.3.3. Resorption features in Site 1183 xenolith crystals

A resorption feature in the Unit 6 xenolith crystal 63R2-X1, identified by texture, included a decrease in An content across the resorption surface towards the rim (i.e., the direction of crystal growth) from An_{85} to An_{81} (see Figs. 2E, 9 and 10). There is no significant change in Mg number of parent magmas across this resorption surface, but there is a decrease in parent magma Ti content. The parent magma of the An_{81} zone, which was the zone grown following resorption, had a higher La/Y and Sr/Ti, although it had less Sr, Ti, and Y, and roughly the same Ba/Sr ratio as the parent magma of the An_{85} zone (see Figs. 9 and 10). A resorption feature in the Unit 7 xenolith crystal 64R2-X1, also identified by texture, included a slight *increase* in An content across the surface from An_{80} to An_{83} (see Fig. 2B). The lower An parent magma (core region) in 64R2-X1 had a higher La/Y and Sr/Ti, and again less Sr, Ti, and Y, with a similar Ba/Sr ratio and Mg# as the An_{83} parent magma. The An_{83} zone was grown following resorption (see Fig. 2B).

6. Discussion

6.1. Inferred chemical magma evolution

6.1.1. Major elements

In terms of An content, the cores of Site 1183 cumulate xenolith plagioclase crystals are generally distinct from the phenocrysts in the host basalt. Sano and Yamashita (2004) suggested that plagioclase in equilibrium with Kwaimbaita magmas should be An_{73-78}. We observed phenocryst zones as low as An_{65} and as high as An_{83}, whereas xenolith interiors were An_{80}–An_{86} (Tables 2 and 3; Figs. 9 and 10). It should, however, be noted that in their experimental studies Sano and Yamashita (2004) observed crystallization of An_{82} plagioclase from Kroenke basalts (parental to Kwaimbaita basalts) at higher temperatures ($\sim 1200\,°C$) and lower pressure (0.1 MPa). Although the Mg# of a residual magma decreases with increased olivine fractionation, we see no evidence of olivine-dominated fractionation in xenolith or phenocryst parent magmas (i.e., no systematic difference of parent magma Mg# between the xenolith crystals and phenocrysts). The ranges of Mg# for parent magmas of both xenolith crystals and phenocrysts overlap the range observed for Kwaimbaita basalts (Fig. 9A; Table 3). Parent magmas of An_{65-79} phenocryst zones from the three Site 1183 basalt units are compositionally similar with regard to Mg number and Ti abundance (e.g., Fig. 9A). This first order observation suggests that they share a common

parent magma, although some lower An phenocryst zones (i.e., 63R2-P4, 59R2-P1, and 59R2-P2) appear to have more evolved parent magmas (Fig. 9). However, when individual units from Site 1183 are considered, the Mg# of the parent magmas changes little with quite a large range in An content (Fig. 10B–D), suggesting that the Mg# is buffered.

Parent magmas of the An-rich xenolith crystals and phenocrysts extend to more primitive compositions than the Kwaimbaita whole-rock composition (Table 2; Fig 9A). This is contrary to the interpretation of Sano and Yamashita (2004) that An-rich zones grew in a relatively evolved and H_2O-rich boundary layer. It is thus necessary to elucidate other factors, in addition to growth in a water-rich boundary layer, which favor crystallization of An-rich plagioclase.

6.1.2. An-rich OJP plagioclase: influence of temperature and pressure

Experimental results have demonstrated that relatively albite-rich plagioclase crystallizes at elevated pressure, and growth of An-rich plagioclase is favored in high temperature magmas at lower pressure (e.g., Grove et al., 1982; Bartels et al., 1991; Vander Auwera et al., 2000; Sano and Yamashita, 2004). We used the MELTS program (Ghiorso and Sack, 1995; Asimow and Ghiorso, 1998) to test the likelihood of equilibrium crystallization of An-rich (i.e., $>An_{82}$) plagioclase at low pressure from relatively hot and primitive OJP magmas. Major elements, H_2O, and other volatile data reported by Roberge et al. (2004) for unaltered Kwaimbaita and Kroenke basaltic glasses from ODP Leg 192 were used as starting compositions for equilibrium crystallization modeling using MELTS (see Table 4). Equilibrium

Table 4
MELTS crystallization modeling of average OJP basalt glasses

Pressure (kbar)	0.1	0.7	1.9
Average Site 1183 Kwaimbaita basaltic glass			
Temperature [a] (°C)	1184	1188	1198
An content [b]	79	79	77
Average Site 1185 Kroenke basaltic glass			
Temperature [a] (°C)	1200	1204	1216
An content [b]	84	83	82
Glass 192-1185B-16R-1, 64			
Temperature [a] (°C)	1217	1222	1229
An content [b]	85	84	84
Average Site 1187 Kroenke basaltic glass			
Temperature [a] (°C)	1200	1206	1218
An content [b]	84	83	82

Glass compositions are from Roberge et al. (2004).
[a] Temperature at which plagioclase starts to crystallize.
[b] Anorthite content of the first-formed plagioclase.

crystallization modeling, which was performed to estimate initial crystallization temperature and An content of plagioclase, was run at 0.1, 0.7, and 1.9 kbar to also explore the influence of pressure on the composition of crystallizing plagioclase. These pressure estimates adhere to previous models that indicate OJP basalts experienced partial crystallization in the shallow crust (<6–8 km depth) (Michael, 1999; Fitton and Goddard, 2004; Roberge et al., 2004; Sano and Yamashita, 2004). Results of MELTS modeling demonstrate average Kroenke basaltic glasses from both Site 1187 and 1185, which are considered to be parental to Kwaimbaita basalt (e.g., Fitton and Goddard, 2004; Sano and Yamashita, 2004), crystallize An_{84} plagioclase at 1200 °C and 0.1 kbar pressure (see modeling results in Table 4). We also modeled crystallization of a single more primitive Kroenke glass with greater MgO, CaO, Al_2O_3 (sample 1185B-15R-1 149 of Roberge et al., 2004), which crystallized An_{85} plagioclase at 1217 °C and 0.1 kbar (Table 4). Indeed, there may be more primitive melts, currently unsampled, that would produce slightly An-richer initial plagioclase (i.e., to account for An_{86} plagioclase from Malaita xenolith ML-X1). The results of the MELTS numerical simulations suggest that equilibrium crystallization in a low-pressure (i.e., ≤ 1 kbar), high-temperature (>1200 °C) crystallization environment favors An-rich plagioclase growth from known compositions of magmas parental to Kwaimbaita basalt.

6.1.3. An-rich OJP plagioclase: influence of water

Sano and Yamashita (2004) invoked a role for water in the genesis of low-MgO, An-rich OJP plagioclase crystals, which they envisaged to form in a water-rich (and presumably incompatible trace element-rich) crystal mush layer. Their interpretation is consistent with the hydrous experimental data of Sisson and Grove (1993). However, while the plagioclase observed by Sisson and Grove (1993) grown in H_2O saturated parent magmas were low-MgO and An-rich, the crystals they observed were more An-rich (generally $\geq An_{90}$) and had lower MgO (<0.2 wt.% MgO) than OJP plagioclase crystals (<An_{90}, and >0.2 wt.% MgO) reported in this study or by Sano and Yamashita (2004) (Table 1). Plagioclase data from the anhydrous experiments of Grove et al. (1982) and Bartels et al. (1991) produced a negative correlation of MgO with An content, which was also documented for OJP plagioclase xenolith crystals and phenocrysts (Sano and Yamashita, 2004; this study; Fig. 8). The experiments of Bartels et al. (1991) were run at 10–20 kbar, and the experiments of Grove et al. (1982) run at 10^{-3} kbar. The lower pressure

experiments of Grove et al. (1982) produced crystals with MgO and An contents similar to natural OJP plagioclase observed in this study and by Sano and Yamashita (2004). While we cannot rule out the influence of H_2O, MELTS modeling and previous experimental studies provide evidence that crystallization of low-MgO, An-rich OJP plagioclase from low-pressure, high-temperature magmas can account for our observations without a significant role for H_2O.

It is, however, impossible to determine unequivocally the roles of H_2O, pressure, and temperature on the genesis of low-MgO, An-rich OJP plagioclase based solely upon major element data. Plagioclase parent magma trace element compositions allow us to further test the contrasting hypotheses that An-rich crystals grew from relatively primitive magmas vs. evolved H_2O-rich magmas.

6.1.4. Trace elements

The relatively low incompatible trace element abundances in the calculated parental magmas, relative to the whole-rock basalt compositions, indicate that crystal fractionation had not occurred to any significant degree and, thus, cannot be invoked as a process to elevate the water content of the magma. Therefore, if water-rich magmas were responsible for An-rich plagioclase crystallization, the magma(s) would need to have been derived from a relatively water-rich source. However, the data from Roberge et al. (2004) indicate this was not the case. As an alternative to growth in an H_2O-rich magma, we suggest that An-rich plagioclase, whether xenolith or phenocryst, crystallized from relatively primitive magmas in the shallow portions of the OJP magma chamber system. This interpretation reconciles the relatively primitive parent magma compositions (i.e., lower incompatible element abundances at a given Mg#; see Fig. 9A) of the An-rich portions of OJP xenolith crystals and phenocrysts.

Extensive plagioclase crystallization depletes a residual melt of Sr, as D_{Sr} in plagioclase is generally >1.2 (see Table 2). In an environment where plagioclase is the dominant crystallizing phase, early formed crystals will contain higher Sr/Ti and lower Ba/Sr ratios, since D_{Ba} and D_{Ti} <1 in plagioclase. In a confined, non-turbulent environment components rejected by growing plagioclase crystals spawn local oversaturations of components needed for later stage clinopyroxene crystallization (e.g., Marsh, 1996). As clinopyroxene crystallizes the incompatibility of La in clinopyroxene relative to Y results in relative depletion of Y and enrichment of La, which will yield a higher La/ Y residual liquid (e.g., Table 2; Fig. 9B–C). Since the

trace elements considered here are highly incompatible in olivine, crystallization of this phase yields minimal change in the ratios of any of these elements (cf. Bindeman et al., 1998; Bindeman and Davis, 2000).

Trace element enrichments and depletions not encountered in whole-rock basalt data include: (1) An$_{80-86}$ xenolith and phenocryst zones that were derived from parent magmas with greater Sr, Y, and Eu, lower La/Y and Ba/Sr, and lower Ba and LREE abundances extending to overall more primitive compositions than whole-rock data (Fig. 9; Table 2). These compositional characteristics suggest that parent magmas of the An-rich zones experienced less clinopyroxene and plagioclase crystallization than lower An zones (Fig. 9). The resorption feature in the Unit 7 xenolith 64R2-X1 provides textural and chemical evidence of exposure to more primitive magma, where the parent magma of the zone grown after resorption is more An-rich, has lower La/Y, and has greater Sr and Y abundances (Figs. 2B, 9 and 10). (2) An$_{65-79}$ phenocryst and xenolith exterior zones with lower Sr, Y, and Eu, higher La/Y and Ba/Sr, and higher Ba and LREE abundance parental magma compositions that extend to more evolved compositions than whole-rock data (Figs. 9 and 10). Included in this group are a small number of phenocrysts, a xenolith exterior zone, and a single resorption feature in the Unit 6 xenolith that indicate crystallization from magma(s) that had experienced relatively extreme plagioclase and clinopyroxene fractionation. In Fig. 9A and C, vectors for clinopyroxene and plagioclase crystallization are shown as arrows. Generation of the highest La/Y ratio we observed in a plagioclase parent magma requires significant clinopyroxene fractionation (Fig. 9). These high La/Y, relatively evolved liquids, were parental to portions of both xenolith crystals (i.e., 63R2-X1 resorption feature) and phenocrysts. In Fig 9C the head of the arrow defining the clinopyroxene crystallization vector corresponds to approximately 70% clinopyroxene crystallization in terms of La/Y for the highest MgO Site 1187 Kroenke basalt reported by Fitton and Goddard (2004). However, the amount of crystallization required to account for trace element variations may be much less given the combined error of calculated partition coefficients (which is larger for Y than La, Ba, Sr, or Ti), LA–ICP–MS analyses, crystallization temperature, pressure, magmatic H$_2$O, and uncertainties regarding bulk D_Y and D_{La} for clinopyroxene (see error bars in Figs. 9 and 10 and the captions of Figs. 7, 9 and 10 for details on how the error bars were estimated).

The observed major and trace element variations require magmas both more and less evolved than those represented by the whole-rock/groundmass. The evolution of these liquids involved crystallization that was dominated early by plagioclase and olivine (as suggested by whole-rock and basaltic glass studies) (e.g., Fig. 9), although as noted above, evidence of olivine fractionation is difficult to identify from the plagioclase trace element data presented here (Neal et al., 1997; Michael, 1999; Tejada et al., 2002, 2004; Roberge et al., 2004; Sano and Yamashita, 2004). Late stage clinopyroxene crystallization also played a significant role in evolution of OJP basaltic magmas, as indicated by variations in La/Y ratios between magma parental to the high and low An zones. Crystallization of plagioclase from high temperature, relatively primitive anhydrous magmas at low pressure was an important process. Conditions to produce the spectrum of relatively evolved and primitive magma compositions recorded in OJP plagioclase are not fully met in a homogenous magma body and require more confined environments such as a crystal mush layers (e.g., Langmuir, 1989; Marsh, 1996; Sano and Yamashita, 2004).

6.1.5. OJP magma chambers, mush layers, and solidification fronts

Sano and Yamashita (2004) suggested that zoned plagioclase, clinopyroxene, and olivine crystals in Kwaimbaita basalts formed as they moved between crystal mush boundary layers (solidification fronts) and the main magma body. Boundary mush layers are rheological elements of multiply saturated solidification fronts defined as having crystallinities between 25% and 50–55% (Marsh, 1996). Crystallization within the mush zone produces interstitial melts that are evolved relative to the magma in the chamber interior, and continued crystallization traps these evolved melts within the solidification front (Langmuir, 1989; Marsh, 1996). Mineral phases with compositions out of equilibrium with main magma body grow within the mush zone of the solidification front where they are thermally and mechanically insulated from the hotter magma chamber interior (Langmuir, 1989). Early formed crystals that potentially contain chemical signatures of relatively primitive magmas may also exist in the rigid crust of the solidification front near the solidus. Solidification fronts thicken over time due to crystal nucleation and growth but may also thicken by capturing crystals carried within new batches of magma. Capture of crystals by the advancing solidification front is greatest along the magma chamber floor due to crystal settling, and the thickness of these cumulates in any given magma chamber may grow to be quite large if repeated transit

and storage of crystal carrying magmas occurs from other magma chambers (Marsh, 1996). Crystal debris may be mobilized from "mushy" cumulate layers and solidification fronts by erosion, density and convection driven plumes, or stirring by new magma input (Marsh, 1996; Kuritani, 1998).

In the case of the OJP magma chamber system, magma in the chamber interior(s) was the most eruptible, had Kwaimbaita or Kroenke basalt-like composition(s), and made up the most significant compositional and textural fractions of basalts erupted to the surface. Disruption of solidification fronts released evolved material (liquid+crystals) to mix with the main body of magma (e.g., Marsh, 1996). Mixing small fractions of evolved material from disrupted solidification fronts into the main magma body can lead to changes in basalt chemistry (Marsh, 1996). However, if the geometry of the OJP magma chamber system was such that inputs from disrupted solidification fronts were small relative to the size of the magma body, the input of more evolved material would have had little affect on the bulk magma chemistry. Evidence for this process is thus best preserved by allochthonous crystals (e.g., Marsh, 1996; Davidson et al., 2005), much like the An_{65-73} phenocrysts with evolved parent magma compositions and the An_{80-86} xenolith crystals with primitive magma compositions, which are all out of equilibrium with the host Kwaimbaita basalt.

Parent magma trace element compositions of An_{65-73} phenocryst zones, which trend to much more evolved compositions than whole-rock data, suggest that some of these crystals grew deep within solidification fronts that were eroded and mixed into the main magma body. Crystals with similarly evolved compositions may also form in dikes and conduits within the magma chamber system that become readily congested. In these regions geometry and magma supply rate allow solidification fronts to propagate inward and meet filling the space with a crystal mush that has a network of interstitial spaces filled with variably evolved melts (Marsh, 1996). Within the interstices of the crystal mush, significant melt differentiation can occur where the mush is infrequently flushed with new (primitive) melt. We suggest that the xenolith crystals and phenocrysts with relatively evolved parent magmas originated from these types of environments (e.g., phenocryst 63R2-P4; phenocryst zones 59R2-P1 core) or were exposed to liquids flushed from these types of environments (e.g., 59R2-P2 rim; xenolith zones 59R2-X1 and 63R2-X1).

Anorthite-rich plagioclase crystals from the cumulate xenoliths grew from relatively primitive magmas that ascended and partially crystallized in shallow magma chambers. Contraction of the clinopyroxene stability field at lower pressures, coupled with evidence of less clinopyroxene fractionation in parent magmas of An-rich zones and results of MELTS simulations, suggests that crystallization of OJP magmas at low pressure was dominated by plagioclase±olivine. Farnetani et al. (1996) also suggested that shallow crystallization of OJP magmas was largely plagioclase and olivine with lesser amounts of late crystallizing clinopyroxene. This relationship is favored by the textures of Site 1183 xenoliths, where partially resorbed clinopyroxene crystals were present in voids within interlocking plagioclase crystals (e.g., Fig. 2C). Given the size of the xenoliths (Figs. 2A and 3A) and their apparent low porosity, they are likely pieces of the deepest and earliest formed portion of the solidification front. The large size and general round nature of plagioclase cumulate xenoliths in Kwaimbaita-type basalt qualitatively suggest that magma delivery and eruption processes were quite vigorous. Vigorous input of magma into the chamber promotes heavy erosion of solidification fronts and deep stirring of cumulates along the chamber floor. We suggest that solidification front disruption was a ubiquitous process over large vertical and lateral scales, which freed both more evolved phenocrysts and less evolved xenoliths to mix with Kwaimbaita-like magma in the chamber interior. The volume fraction of material from disrupted solidification fronts generally was probably small (i.e., as suggested by <2% phenocrysts by volume; Sano and Yamashita, 2004), and thus did not significantly change bulk magma chemistry, unless extensive resorption of crystals occurred.

A laterally and vertically extensive system of interconnected dikes and sills with regions dominated by liquid and other regions dominated with a crystal–liquid mush can account for the zoning and compositional features recorded in OJP xenolith and phenocryst plagioclase crystals (see Fig. 11). Oscillatory zoned crystals may have formed in a quiet environment where feedback between the rate of crystal growth and diffusion in a boundary layer at the crystal-melt growth interface yielded small and frequent variations of melt composition near the growing crystal (Allegre et al., 1981; Pearce, 1994; Wallace and Bergantz, 2005; (Figs. 2, 3 and 5)). Oscillatory zoned crystals may have also formed where small and frequent variations in melt composition and/or temperature were produced by convection of the main magma body at the inward edge of the solidification front (e.g., Ginibre et al., 2004). Indeed, where magma recharge is frequent, solidification front growth can be arrested or reversed
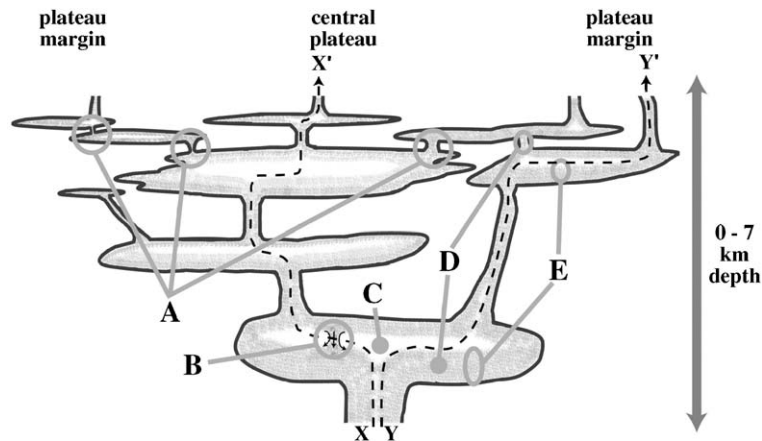
Fig. 11. This is a simplified schematic of the Ontong Java Plateau magma chamber system consisting of a series of interconnected dikes and sills similar to the mush-column magma chamber model of Marsh (1996) in the 0 to 7km depth range. Magma ascending magma chamber system that follows the path (dashed line) X–X′ is subject to more density filtration (i.e., in the center of the plateau). Magma that ascends along the path (dashed line) Y–Y′ is subject to less density filtration, hence a wide variety of magma types are erupted along this path (i.e., along the plateau margins). (A) Due to geometry, these areas quickly become congested via crystallization during period of low magma throughput. Interstitial fluids in these regions, within the congested crystal–liquid mush, experience greater degrees of fractionation. (B) Solidification front material may dislodge from the roof and cascade as a plume of liquid+crystals with components both in and out of equilibrium with the main magma body. Some of this material may escape to be carried to the surface. (C) Liquid-dominated regions of the magma chamber, which are also the hottest portions of the system. In the OJP magma chamber system, this was filled with Kwaimbaita and/or Kroenke-type magmas. (D) Examples of crystal (or crystal mush) dominated zones, where within the mush evolved liquids are present. Crystal phases out of equilibrium with the main magma body are also present in these zones, where their growth environment is thermally and mechanically insulated from the hot chamber interior (e.g., Marsh, 1996). (E) Thick solidification fronts along chamber floors (i.e., cumulate layers). These crystal mush cumulate layers thickened with the repeated input of crystal-bearing magmas.

placing deeper zones of the front in repeated contact with fresh primitive melt (Marsh, 1996). We have noted evidence that magma recharge was both vigorous and frequent to have generated the most of the volume of the OJP around ∼122Ma. In the case of a shallow OJP magma chamber, frequent and vigorous recharge would favor production of oscillatory zoned An-rich plagioclase crystallizing from relatively primitive parental magmas, whereas a stagnant environment would favor production of oscillatory zoned An-poor plagioclase crystallizing from more evolved parental melts. Thick cumulate mush layers along the floors of OJP magma chambers were also likely important in the widespread genesis of Kwaimbaita basalt (e.g., Fig. 11). An important factor in basalt differentiation in the crystal mush dominated portions of the magmatic system would have been the residence time of melts within the vertically and laterally extensive crystal mush network (Marsh, 1996; Fig. 11). Near steady-state supply of magma into the system (e.g., Resmini and Marsh, 1995) would have resulted in tightly constrained basalt compositions consistent with Kwaimbaita-type basalts that make up the bulk of the OJP. Given the size of the OJP, persistent melting over the lifetime of the causative thermal disturbance is amenable to near steady-state melt infiltration of the mush-column-type

OJP magma chamber system as illustrated in Fig. 11 (e.g., Marsh, 1996).

Shallow OJP magma evolution was thus influenced by a balance of several processes that included: (1) formation of evolved melts within crystal mush dominated regions; (2) flushing of variably evolved melts from the crystal mush and homogenization of these melts within the main magma body; (3) entrainment of phenocrysts and other crystal debris (e.g., An-rich xenoliths) during magma recharge; (4) resorption (partial or complete) of crystal debris; (5) crystal settling, and (6) input of new, primitive magma (see Fig. 11). Partial crystallization of magmas at depths of 0–7km, within the range suggested for the OJP, coincides with zones of neutral buoyancy as discussed by Ryan (1987). Studies have suggested that the OJP crust contains significant gabbro and/or dolerite intrusions that would have corresponded to zones of neutral buoyancy and a large shallow magma chamber system during active OJP volcanism (e.g., Farnetani et al., 1970, 1976, 1996; Hussong et al., 1979; Neal et al., 1997). Widespread gabbro and dolerite intrusions are consistent with our interpretation that the OJP magma chamber system consisted of interconnected crystal mush-rich magma chambers. Ryan (1987) suggested that as crust is thickened by erupted lavas, the zone of neutral buoyancy

will slowly migrate upward. Slow upward migration of the magma chamber system would favor slow yet pervasive assimilation of overlying rock, potentially seawater-altered basalts in the case of the OJP. Indeed, Michael (1999) and Roberge et al. (2004) suggested that assimilation of seawater-altered basalt or materials with a seawater brine component as the source of widespread Cl contamination of OJP basaltic glasses. Additionally, Neal and Davidson (1989) invoked seawater-altered basalt as the contaminant to the parental magma that produced megacrysts entrained in post-OJP alnöite pipes on Malaita, Solomon Islands. However, we note that the assimilation of such a seawater-altered component did not radically elevate the water content of the magma within the different chambers.

Magma chambers are more sheet-like near the Earth's surface (Marsh, 1989). The maximum vertical extent of interconnected sheet-like chambers would have been where the supply of intruding magma was the greatest (i.e., toward the center of the plateau; Fig. 11). The total integrated thickness of the dike and sill system was thus less along the margins of the OJP, which allowed magmas distinct from Kwaimbaita-type to ascend through the mush column and erupt (see Fig. 11). Indeed, the greatest compositional diversity is observed along the plateau margins (e.g., Mahoney et al., 1993a,b, 2001; Fitton and Goddard, 2004). Along the thinner margins of the plateau the magma chamber system and overlying rock would have acted as less of a density filter than the thicker central portion of the plateau (Fig. 11). We calculated average OJP magma densities using the KWare Magma program written by Dr. Ken Wohletz using the glass compositions reported by Michael (1999) and Roberge et al. (2004) at a temperature of 1180 °C and a pressure of 1 kbar (KWare Magma program is available at http://geont1.lanl.gov/Wohletz/Magma.htm). It would have been possible for more (e.g., Kroenke-type: $2869 \pm 3 \, kg/m^3$) and less dense (Singgalo-type: $2860 \, kg/m^3$ and Kwaimbaita-type: $2861 \pm 3 \, kg/m^3$) magmas to ascend the mush pile and reach the surface along the margins of the plateau where there was less overlying volume of intruded and extruded magma. Indeed, Kroenke basalt flows are found to be stratigraphically above Kwaimbaita basalt at Site 1185 of ODP Leg 192 (Mahoney et al., 2001). Although the magma chamber system may have been thinner along the margins of the plateau, variations in magma residence time in the system did not *preclude* formation and eruption of Kwaimbaita magmas along the OJP margins. Differences, however slight, in the densities of Kroenke, Kwaimbaita, and Singgalo magmas would have lead to different rates and patterns

of magma ascent, pooling, and crystallization en route to the surface.

7. Summary and conclusions

Anorthite-rich (An_{80-86}) portions of plagioclase crystals from cumulate xenoliths and phenocrysts in host basalts were formed primarily by crystallization in shallow (low pressure, 2–7 km depth) regions of the OJP magma chamber system from more primitive magmas than those basalts sampled from the OJP that were low in H_2O and at relatively high temperature (liquidus temperature near 1200 °C). Evidence from this study shows that the role of H_2O-rich evolved boundary layer interstitial melts in the formation of An-rich plagioclase was, at best, minor. Parent liquid compositions derived from OJP xenolith and phenocryst plagioclase crystals contain a wider compositional record of magma evolution than that revealed by OJP whole-rock basalt data. Cumulate xenoliths and phenocrysts generally are pieces of disrupted solidification fronts. Solidification fronts would have been ubiquitous throughout the OJP magma chamber system. The OJP magma chamber system was composed of interconnected dikes and sills and consisted of regions dominated by liquid (magma chamber interior) and regions dominated by crystal–liquid mush (along magma chamber floors and walls, within dikes and conduits). Crystals and crystalline debris were extensively recycled throughout the OJP magma chamber system. This recycling accounts for the wide compositional spectrum of magmas parental to plagioclase xenolith crystals and phenocrysts with An content out of equilibrium with their Kwaimbaita host basalts. Ironically, this process also accounts for the dominance of a single magma composition erupted on to the OJP, as it represents the homogenized body of magma in the main part of the upper chamber.

The compositions of melts periodically flushed from the interstices of the crystal mush network were affected by their residence times in the mush. Depending upon the extent of the crystal-rich portions of the magma chamber system, residence time may have had a large effect on overall basalt chemistry. The shallow crustal OJP magma chamber system corresponded with a zone of neutral buoyancy in the 0–7 km depth range, as in other volcanic systems (Ryan, 1987). As OJP volcanism progressed the plateau gained elevation, and the zone of neutral buoyancy gradually migrated upward leading to slow yet pervasive assimilation of overlying seawater-altered basalt.

The greatest diversity of OJP basalts is along the margins of the plateau where it is thinner. During

formation, magmas ascending into the marginal and thinner magma chamber system around the plateau margins were subject to less density filtration, which allowed ascent and eruption of relatively dense Kroenke magmas and slightly less dense Singgalo magmas (see Fig. 1 for magma types and distribution across the OJP). Slight variations in paths of magma ascent, depths of magma pooling and crystallization, as well as rates and amounts of assimilation of seawater-altered basalt would have affected the isotopic and incompatible trace element characteristics of known OJP basalts. We suggest that these physical factors may account for both the homogeneity of basalts in the central portion of the OJP and the relative heterogeneity of basalts around the plateau margin.

Acknowledgements

Appendix A. Supplementary data

Supplementary data associated with this article can be found, in the online version, at doi:10.1016/j.jvolgeores.2005.09.024.

References

Allegre, C.J., Provost, A., Jaupart, C., 1981. Oscillatory zoning: a pathological case of crystal growth. Nature 294, 223–228.

Asimow, P.D., Ghiorso, M.S., 1998. Algorithmic modifications extending MELTS to calculate subsolidus phase relations. Am. Mineral. 83, 1127–1131.

Bartels, K.S., Kinzler, R.J., Grove, T.L., 1991. High pressure phase relations of primitive high-alumina basalts from Medicine Lake volcano, northern California. Contrib. Mineral. Petrol. 108, 253–270.

Bindeman, I.N., Bailey, J.C., 1999. Trace elements in anorthite megacrysts from the Kurile Island Arc: a window to across-arc geochemical variations in magma compositions. Earth Planet. Sci. Lett. 169, 209–226.

Bindeman, I.N., Davis, A.M., 2000. Trace element partitioning between plagioclase and melt: investigation of dopant influence on partition behavior. Geochim. Cosmochim. Acta 64, 2863–2878.

Bindeman, I.N., Davis, A.M., Drake, M.J., 1998. Ion microprobe study of plagioclase–basalt partition experiments at natural concentration levels of trace elements. Geochim. Cosmochim. Acta 62, 1175–1193.

Blundy, J., 1997. Experimental study of a Kiglapait marginal rock and implications for trace element partitioning in layered intrusions. Chem. Geol. 141, 73–92.

Blundy, J.D., Wood, B.J., 1991. Crystal-chemical controls on the partitioning of Sr and Ba between plagioclase feldspar, silicate melts, and hydrothermal solutions. Geochim. Cosmochim. Acta 55, 193–209.

Bryce, J.G., DePaolo, D.J., 2004. Pb isotopic heterogeneity in basaltic phenocrysts. Geochim. Cosmochim. Acta 68, 4453–4468.

Chambers, L.M., Pringle, M.S., Fitton, J.G., 2002. Age and duration of magmatism on the Ontong Java Plateau: ^{40}Ar–^{39}Ar results from ODP Leg 192. Abstract V71B-1271, Eos, Trans. - Am. Geophys. Union 83, F47.

Coffin, M.F., Eldholm, O., 1994. Large igneous provinces: crustal structure, dimensions, and external consequences. Rev. Geophys. 32, 1–36.

Coffin, M., Pers. comm., 2003.

Davidson, J.P., Tepley III, F.J., Knesel, K.M., 1998. Isotopic fingerprinting may provide insights into evolution of magmatic systems. EOS Trans. AGU 79, 185,189,193.

Davidson, J.P., Hora, J.M., Garrison, J.M., Dungan, M.A., 2005. Crustal forensics in arc magmas. J. Volcanol. Geotherm. Res. 140, 157–170.

Deer, W.A., Howie, R.A., Zussman, J., 2001. Rock-Forming Minerals: Framework Silicates Feldspars, vol. 4A. 2nd ed. The Geological Society of London.

Eggins, S.M., Shelley, J.M.G., 2002. Compositional heterogeneity in NIST SRM 610–617 glasses. Geostand. Newsl. 26 (3), 269–286.

Farnetani, C.G., Richards, M.A., Ghiorso, M.S., 1996. Petrological models of magma evolution and deep crustal structure beneath hotspots and flood basalt provinces. Earth Planet. Sci. Lett. 143, 81–94.

Fitton, J.G., Goddard, M., 2004. Origin and evolution of magmas on the Ontong Java Plateau. In: Fitton, J.G., Mahoney, J.J., Wallace, P.J., Saunders, A.D. (Eds.), Origin and Evolution of the Ontong Java Plateau. Geological Society, Special Publications, London, vol. 229, pp. 151–178.

Furomoto, A.S., Hussong, D.M., Campbell, J.F., Sutton, G.H., Malahoff, A., Rose, J.C., Woollard, G.P., 1970. Crustal and upper mantle structure of the Solomon Islands as revealed by seismic refraction survey of November–December 1966. Pac. Sci. 24, 315–332.

Furomoto, A.S., Webb, J.P., Odegard, M.E., Hussong, D.M., 1976. Seismic studies of the Ontong Java Plateau, 1970. Tectonophysics 34, 71–90.

Ghiorso, M.S., Sack, R.O., 1995. Chemical mass transfer in magmatic processes: IV. A revised and internally consistent thermodynamic model for interpolation and extrapolation of liquid–solid equilibria in magmatic systems at elevated temperatures and pressure. Contrib. Mineral. Petrol. 119, 197–212.

Ginibre, C., Wörner, G., Kronz, A., 2002. Minor- and trace-element zoning in plagioclase: implications for magma chamber processes at Parinacota volcano, northern Chile. Contrib. Mineral. Petrol. 143, 300–315.

Ginibre, C., Wörner, G., Kronz, A., 2004. Structure and dynamics of the Laacher See magma chamber (Eifel, Germany) from major and trace element zoning in sanidine: a cathodoluminescence and electron microprobe study. J. Petrol. 45, 2197–2223.

Grove, T.L., Gerlch, D.C., Sando, T.W., 1982. Origin of calc-alkaline series lavas at Medicine Lake volcano by fractionation, assimilation, and mixing. Contrib. Mineral. Petrol. 80, 160–182.

Hussong, D.M., Wipperman, L.K., Kroenke, L.W., 1979. The crustal structure of the Ontong Java and Manihiki oceanic plateaus. J. Geophys. Res. 84, 6003–6010.

Jefferies, T.E., Jackson, S.E., Longerich, H.P., 1998. Application of a frequency quintupled Nd:YAG source ($\lambda=213\,nm$) for laser ablation inductively coupled plasma mass spectrometric analysis of minerals. J. Anal. At. Spectrom. 13, 935–940.

Kroenke, L.W., Berger, W.H., Janecek, T.R., et al., 1991. Proc. ODP Init. Repts., Leg, vol. 130. Ocean Drilling Program, College Station, TX.

Kuritani, T., 1998. Boundary layer crystallization in a basaltic magma chamber: evidence from Rishiri Volcano, Northern Japan. J. Petrol. 39, 1619–1640.

Langmuir, C.H., 1989. Geochemical consequences of in situ crystallization. Nature 340, 199–205.

Longerich, H.P., Jackson, S.E., Günther, D., 1996. Laser ablation inductively coupled plasma mass spectrometric transient signal data acquisition and analyte concentration calculation. J. Anal. At. Spectrom. 14, 1363–1368.

Longhi, J., Walker, D., Hays, J.F., 1976. Fe and Mg in plagioclase. Proc. 7th. Lunar Planet. Sci. Conf. 1281–1300 (L4).

Mahoney, J.J., Storey, M., Duncan, R.A., Spencer, K.J., Pringle, M., 1993a. Geochemistry and age of the Ontong Java Plateau. In: Pringle, M.S., Sager, W.W., Sliter, W.V., Stein, S. (Eds.), The Mesozoic Pacific: Geology, Tectonics, and Volcanism. Geophys. Monogr., vol. 77. A.G.U, Washington, DC, pp. 233–262.

Mahoney, J.J., Storey, M., Duncan, R.A., Spencer, K.J., Pringle, M., 1993b. Geochemistry and geochronology of Leg 130 basement lavas: nature and origin of the Ontong Java Plateau. In: Berger, W.H., Kroenke, L.W., Mayer, L.A., et al. (Eds.), Proceedings of the Ocean Drilling Program, Scientific Results, vol. 130.

Mahoney, J.J., Fitton, J.G., Wallace. P.J., et al., 2001. Basement drilling of the Ontong Java Plateau, Sites 1183–1187, 8 September–7 November, 2000. Proc. ODP Init. Rpts., 192, [Online] Available from world wide web: http://www-odp.tamu.edu/publications/192_IR/192ir.htm.

Marsh, B.D., 1989. Magma chambers. Annu. Rev. Earth Planet. Sci. 17, 439–474.

Marsh, B.D., 1996. Solidification fronts and magma dynamics. Mineral. Mag. 60, 5–40.

Michael, P.J., 1999. Implications for magmatic processes at Ontong Java Plateau from volatile and major element contents of Cretaceous basalt glasses. Geochem. Geophys. Geosyst. 1 (1999GC000025).

Neal, C.R., Davidson, J.P., 1989. An unmetasomatized mantle source for the Malaitan alnöite (Solomon Islands): petrogenesis involving zone refining, megacryst fractionation, and assimilation of oceanic lithosphere. Geochim. Cosmochim. Acta 53, 1975–1990.

Neal, C.R., Mahoney, J.J., Kroenke, L.W., Duncan, R.A., Petterson, M.G., 1997. The Ontong Java Plateau. In: Mahoney, J.J., Coffin,

M.F. (Eds.), Large Igneous Provinces: Continental, Oceanic, and Planetary Flood Volcanism. Geophysical Monograph, vol. 100. American Geophysical Union, pp. 183–216.

Norman, M.D., Pearson, N.J., Sharma, A., Griffin, W.L., 1996. Quantitative analysis of trace elements in geological materials by laser ablation ICP-MS: instrumental operating conditions and calibration values of NIST glasses. Geostand. Newsl. 20, 247–261.

Pearce, T.H., 1994. Recent work on oscillatory zoning in plagioclase. In: Parsons, I. (Ed.), Feldspars and their Reactions, vol. 421. Kluwer Academic, London, pp. 313–350.

Petterson, M.G., Neal, C.R., Mahoney, J.J., Kroenke, L.W., Saunders, A.D., Babbs, T.L., Duncan, R.A., Tolia, D., McGrailo, B., 1997. Structure and deformation of north–central Malaita, Solomon Islands: tectonic implications for Ontong Java Plateau–Solomon arc collision, and for the fate of oceanic plateaus. Tectonophysics 283, 1–33.

Phinney, W.C., 1994. Partition coefficients for iron between plagioclase and basalt as function of oxygen fugacity: implications for lunar anorthosites. Geochim. Cosmochim. Acta 56, 1885–1895.

Resmini, R.G., Marsh, B.D., 1995. Steady-state volcanism, paleoeffusion rates, and magma system volume inferred from plagioclase crystal size distributions in mafic lavas: Dome Mountain, Nevada. J. Volcanol. Geotherm. Res. 68, 273–296.

Roberge, J., White, R., Wallace, P., 2004. Volatiles in submarine basaltic glasses from the Ontong Java Plateau (ODP Leg 192): implications for magmatic processes and source region compositions. In: Fitton, J.G., Mahoney, J.J., Wallace, P.J., Saunders, A.D. (Eds.), Origin and Evolution of the Ontong Java Plateau. Geological Society, Special Publications, London, vol. 229, pp. 239–257.

Ryan, M.P., 1987. Neutral buoyancy and the mechanical evolution of magmatic systems. In: Mysen, B.O. (Ed.), Magmatic Processes: Physicochemical Principles. The Geochemical Society Spec. Publ., vol. 1, pp. 259–288.

Sano, T., Yamashita, S., 2004. Experimental petrology of basement lavas from Ocean Drilling Program Leg 192: implications for differentiation processes in Ontong Java Plateau magmas. In: Fitton, J.G., Mahoney, J.J., Wallace, P.J., Saunders, A.D. (Eds.), Origin and Evolution of the Ontong Java Plateau. Geological Society, Special Publications, London, vol. 229, pp. 185–218.

Sisson, T.W., Grove, T.L., 1993. Experimental investigations of the role of H_2O in calc-alkaline differentiation and subduction zone magmatism. Contrib. Mineral. Petrol. 113, 143–166.

Smith, J.V., Brown, W.L., 1988. Feldspar Minerals, vol. 1. Springer-Verlag.

Tarduno, J.A., Sliter, W.V., Kroenke, L., Leckie, M., Mayer, H., Mahoney, J.J., Musgrave, R., Storey, M., Winterer, E.L., 1991. Rapid formation of Ontong Java Plateau by Aptian mantle plume volcanism. Science 254, 399–403.

Tejada, M.L.G., Mahoney, J.J., Duncan, R.A., Hawkins, M.P., 1996. Age and geochemistry of basement and alkalic rocks of Malaita and Santa Isabel, Solomon Islands, southern margin of the Ontong Java Plateau. J. Petrol. 37, 361–394.

Tejada, M.L.G., Mahoney, J.J., Neal, C.R., Duncan, R.A., Petterson, M.G., 2002. Basement geochemistry and geochronology of Central Malaita, Solomon Islands, with implications for the origin and evolution of the Ontong Java Plateau. J. Petrol. 43, 449–484.

Tejada, M.L.G., Mahoney, J.J., Castillo, P.R., Ingle, S.P., Sheth, H.C., Weis, D., 2004. Pin-pricking the elephant: evidence on the origin of the Ontong Java Plateau from Pb–Sr–Hf–Nd isotopic characteristics of ODP Legs 192 basalts. In: Fitton, J.G., Mahoney,

J.J., Wallace, P.J., Saunders, A.D. (Eds.), Origin and Evolution of the Ontong Java Plateau. Geological Society, Special Publications, London, vol. 229, pp. 133–150.

Tepley III, F.J., Davidson, J.P., Tilling, R.I., Arth, J.G., 2000. Magma mixing, recharge and eruption histories recorded in plagioclase phenocrysts from El Chichón Volcano, Mexico. J. Petrol. 41, 1397–1411.

Vander Auwera, J., Longhi, J., Duchesne, J.C., 2000. The effect of pressure on D_{Sr} (plag/melt) and D_{Cr} (opx/melt): implications for anorthosite petrogenesis. Earth Planet. Sci. Lett. 178, 303–314.

Wallace, G.S., Bergantz, G.W., 2005. Reconciling heterogeneity in crystal zoning data: an application of shared characteristic diagrams at Chaos Crags, Lassen Volcanic Center, California. Contrib. Mineral. Petrol. 140, 98–112.

Wilke, M., Behrens, H., 1999. The dependence of the partitioning of iron and europium between plagioclase and hydrous tonalitic melt on oxygen fugacity. Contrib. Mineral. Petrol. 137, 102–114.

Wood, B.J., Blundy, J.D., 2002. The effect of H_2O on crystal–melt partitioning of trace elements. Geochim. Cosmochim. Acta 66, 3647–3656.